(1)

学位論文

# STM/STS Studies of Small Metal Particles
# (STM/STSによる金属微粒子の研究)

平成６年１２月博士（理学）申請

東京大学大学院理学系研究科
物理学専攻

内橋　隆

学位論文

# STM/STS Studies of Small Metal Particles
# (STM/STSによる金属微粒子の研究)

平成６年１２月博士（理学）申請

東京大学大学院理学系研究科
物理学専攻

内橋　隆

Thesis

# STM/STS studies of small metal particles

Takashi Uchihashi

Department of Physics
School of Science
University of Tokyo

December 1994

# Contents

# Chapter 1

# Introduction

A small metal particle exhibits interesting properties that are different from those of a bulk metal. In a fine metal particle less than 100 Å in diameter, the kinetic energy level spacings of electron is larger than the life-time width, *i.e.*, discrete at low temperature because of its small volume. Furthermore, such a particle has extremely small self capacitance so that, if an electron is added to or taken out from a particle, a change in electrostatic energy is very large. This prevents a transfer of an electron between the environment and the particle. These two peculiar features lead to anomalous properties of a small metal particle as predicted by Kubo in 1962 [1]. A superconducting fine particle also has interesting properties that a bulk superconductor hardly shows; order parameter thermally fluctuates, because its superconducting condensation energy is comparable to thermal energy [2].

The effect of charging energy, which is important in fine particles, has again attracted attention owing to the advance of submicron fabrication technique in recent years. In tunnel junctions with extremely small area (about $10^{-2}$ $\mu$m$^2$), charging energy of electrons, like in a fine particle, can be large enough that it suppresses electron tunneling at low temperature (the Coulomb blockade of tunneling). In another words, a finite energy larger than the so-called Coulomb gap is required to transfer electrons through junctions. As a consequence, when biased, electron tunnels one by one quasi-periodically, strongly affecting the transport phenomena in the system. The single electron tunneling is one of the main subjects of so-called mesoscopic physics [3].

Scanning tunneling microscopy (STM) can be a useful tool for studying the

two subjects mentioned above. When a STM tip probes a metal particle deposited on a substrate, a tunnel junction is formed between the tip and the particle. This tunnel junction can be sufficiently small to investigate the single electron tunneling [4]. Indeed, many groups have used STM to observe it. The STM also has a great potential for measuring electronic properties of a fine particle by the method of tunneling spectroscopy (STS). However, the STM method on this subject has not been done. This is probably because the Coulomb blockade, which suppresses tunnel current around zero bias voltage, prevents the electronic properties of a particle to be observed.

We have studied properties of fine particles and single electron tunneling using STM. The Coulomb blockade of tunneling was studied for normal-metal particles. For superconducting particles, we found a transition from the Coulomb gap to the superconducting energy gap. Electronic properties of a particle were also studied, with an emphasis on fluctuation of order parameter.

The present thesis is organized as follows. In Chapter 2, we review past experiments and theories related to our three subjects: fine particles, STM, and single electron tunneling. Chapter 3 describes the details of the STM used in this experiment. In chapter 4, sample preparation and measurement methods are given. Chapter 5 is devoted to the results of the experiment and discussion. Last, in Chapter 6 we summarize the experiment.

# Chapter 2

# Review of Theories and Experiments

## 2.1 Fine Particles

In 1962 Kubo predicted that properties of a small metal particle much differs from those of a bulk metal [1]. Since then, this field has attracted many people for a long time. In this section we briefly review normal and superconducting fine particles.

### 2.1.1 The Kubo Effect

In a bulk metal the electron energy spectrum is usually considered to be continuous despite its finite volume. This is because finite life time of energy levels caused by electron-phonon scattering smoothes out the energy spectrum. However, in a sufficiently small particle , the assumption of continuous energy spectrum is no longer valid. The mean energy-level spacing $\delta$ of a fine particle is written by

$$\delta = 1/N(0)V, \tag{2.1}$$

where $N(0)$ is the density of states per unit volume at the Fermi level, and $V$ the volume of the particle. For example, for an aluminum fine particle with a diameter of 100 Å, $\delta/k_B = 1.3$ K. Hence, it is expected that electronic properties of a fine particle are affected by finite energy level spacings at low temperature [1].

Another important effect arising from smallness of volume is that a fine particle is electrically neutral [1]. When one electron is added to or subtracted from an electrically neutral particle with a diameter of $d$, Coulomb energy $U = e^2/d$ is needed. For $d = 100$ Å, $U/k_B$ becomes $10^3$ K, which is much larger than the temperature of liquid helium. This means that the Fermi distribution function cannot be used any more, because it is based on the grand-canonical treatment that assumes a particle reservoir. Phenomena that properties of a fine particle deviate from those of a bulk metal at low temperature are called the Kubo effects (see Fig.2.1.1).

Kubo calculated properties of a fine particle assuming that electron energy levels are randomly distributed. But this is not the case. Gor'kov *et al.* used the random matrix theory and showed that energy levels of a fine particle tend to be equally spaced [5][6]. This is understood if one thinks that energy levels in proximity repulse one another as a result of the second-order energy perturbation.

Let us take the spin susceptibility of a fine particle for example (Fig.2.1.2) [7]. The number of electrons in a fine particle is fixed, being even or odd. If the number is even (even particle), the susceptibility goes to zero as $T$ decreases to zero because a finite energy is needed to excite electrons from the ground state. On the other hand, if the number is odd (odd particle), it goes to infinite as $T$ decreases to zero because little energy is needed to excite electrons (Fig.2.1.3). Thus, the spin susceptibility of a fine particle largely deviates from that of a bulk metal at temperatures lower than $\delta/k_B$. Spin susceptibility is measured from the Knight shift of NMR. Figure 2.1.4 shows an experiment by Kobayashi *et al.* [8], which proved the vanishment of the Knight shift at low temperature. Since their sample is an ensemble of particles, the measured quantity differs from particle to particle. In such a situation, mainly even particles contribute to the average, because their susceptibilities are all nearly equal to zero. Hence, their result reflects the vanishment of spin susceptibility of even particles.



### 2.1.2 Zero Dimensional Superconductor and Thermal Fluctuation

It is widely known that in a bulk superconductor, thermal fluctuation is almost negligible and the transition from normal to superconducting phase is very sharp. This is because the coherence length $\xi$ of a superconductor is very long ($\approx 1000$ Å), so that the mean-field treatment is applicable. In contrast, in a superconducting fine particle less than coherence length $\xi$ in diameter, called zero dimensional superconductor, the mean-field treatment fails near transition temperature. Superconducting condensation energy of such a particle can be comparable to the temperature because of its small volume, so that thermal fluctuation of the order parameter becomes large. Consequently, the phase transition gets smeared, and thermodynamic properties such as specific heat and spin susceptibility are much modified from those of bulk superconductors [2].

To consider the fluctuation effect, we follow the theory by Mühlschlegel *et al.* [9]. For an order parameter $\psi(x)$, the Ginzburg-Landau (GL) free energy of a superconductor is given by

$$F[\psi(x)] = \int d^3x (a|\psi|^2 + \frac{b}{2}|\psi|^4 + c|\nabla\psi|^2), \tag{2.2}$$

where $a = N(0)(T - T_c)/T_c$ and $b = 7\zeta(3)N(0)/8\pi^2(kT_c)^2$. $N(0)$ is the density of states at the Fermi level and $\zeta(3)$ is the $\zeta$ function. Mühlschlegel *et al.* generalized it to calculate properties of a superconducting fine particle. They expressed the partition function $Z$ as a functional integral of $exp(-\beta F[\psi(x)])$ over all order parameter fields $\psi(x)$:

$$Z = \int \delta\psi(x) exp(-F[\psi(x)]/k_BT). \tag{2.3}$$

As is seen from Eq.(2.3), the deviation of order parameter that changes the free energy $F[\psi(x)]$ by $k_BT$ at most contributes to the partition function. In view of their treatment, the GL theory neglects this fluctuation and takes $\psi(x)$ that maximizes the free energy.

Now we estimate the breadth of the critical region, within which fluctuation of order parameter is large enough that the mean-field treatment cannot be applied. In a small particle less than coherence length in diameter, the last term of Eq.(2.2) is negligible and the order parameter $\psi(x)$ is spatially constant. In addition, we can replace $T$ in Eq.(2.3) by $T_c$ near transition temperature. As a result, Eq.(2.3) reduces to a dimensionless form by changing variables $\lambda^{1/2} = |\psi|/\pi k_B T_c$:

$$Z = \pi^3 (k_B T_c)^2 \int_0^\infty d\lambda exp(-\frac{\pi^2}{\bar{\delta}}[-\Delta t\lambda + \bar{b}\lambda^2]) \tag{2.4}$$

with

$$\bar{\delta} = 1/N(0)\Omega k_B T_c = \delta/kT_c, \tag{2.5}$$

$$\bar{b} = 0.526, \quad \Delta t = 1 - T/Tc, \tag{2.6}$$

where $\Omega$ is the volume of the particle, and $\delta$ is the mean electron energy spacing in the particle mentioned earlier. The exponent in Eq.(2.4) is shown in Fig.2.1.5 as a function of the dimensionless order parameter $\lambda$. As is seen from the figure, fluctuation of order parameter is estimated to be

$$\frac{\Delta\lambda}{\lambda_{mean}} = \frac{(\bar{\delta}/\bar{b})^{1/2}}{\Delta t/2b} = \frac{2(\bar{\delta}\bar{b})^{1/2}}{\Delta t}. \tag{2.7}$$

Therefore, the critical region $\Delta t$ where fluctuation dominates is about $\bar{\delta}^{1/2}$. Let us consider a particle size relevant to fluctuation. For example, again, for an aluminum fine particle with a diameter of 100 Å, $T_C = 1.2$ K and $\delta = 1.3$ K give $\bar{\delta} \approx 1$. This means that fluctuation is important over the entire temperature region below $T_C$.

Electronic properties of a superconductor can be classified into those of Cooper pairs and quasi particles. Diamagnetic susceptibility is associated with the former, while spin susceptibility with the latter. Hence, one can experimentally investigate the fluctuation effects by observing these quantities. They are expected to deviate from the BCS theory near the transition temperature



when fluctuation dominates this region. Figure 2.1.6 shows the diamagnetic susceptibility of superconducting fine particles measured by Buhrman *et al.* [10], which agrees well with a theoretical prediction by Mühlschlegel *et al.*. In the critical region, a smearing of the transition from normal to superconducting phase is seen. In Fig.2.1.7 the Knight shifts of NMR measured by Ido [11] is shown. They also largely deviate from the BCS theory, showing the presence of fluctuation.

### 2.1.3 Lower Size Limit for Superconductivity

The size dependence of the superconducting energy gap and the transition temperature of fine particles is a question that is not clear yet. Although there has been many studies on this subject, their results are quite different from one another. The differences of surface conditions of fine particles among these experiments seem to complicate this problem.

It is interesting to ask what the lower size limit for superconductivity is. Anderson argued that superconductivity would be destroyed when the mean energy-level spacing $\delta$ became larger than the superconducting energy gap $\Delta$ [12]. This means that the lower size limit is about 70 Å for Al. However, experiments suggest that superconductivity remains when the size is reduced below the Anderson's limit [13]. There is no consensus on this issue to our knowledge.

Let us take the experiment by Zeller and Giaever [14] for example. They carried out tunneling spectroscopy of superconducting fine particles of Sn buried in Sn oxides. The superconducting energy gaps were determined from conductance-voltage characteristics that show suppression around zero bias voltage. Their results are shown in Fig.2.1.8. They concluded that for diameters from 360 Å to 100 Å the energy gap slightly increases with a decrease in size, contrary to a theoretical prediction [15].

## 2.2 Scanning Tunneling Microscopy

In 1983 Binnig *et al.* first observed the 7×7 structure of Si(111) surface with scanning tunneling microscopy (STM) [16]. Since its invention, STM has become a powerful tool for surface investigation, and its application has spread not only in surface physics, but also in many other fields such as cryophysics and biology.

Figure 2.2.1 shows the principle of STM operation. When the STM tip and the sample are close enough that their wave functions of electrons overlap (the separation is about 10-50 Å), a tunnel current flows if a bias voltage is applied between them. The current is, by applying a voltage to the actuator to which the tip is attached, fed back to the tip position so that the current can be kept constant. When the tip is scanned over the surface of the sample, the vertical tip position is adjusted automatically to maintain the constant separation by the feedback system. Since changes in the vertical tip position correspond to the surface structure, a surface image is thus obtained from the tip position, namely, the voltage applied to the actuator.

The tunnel current $I$ follows the relation:

$$I \propto \exp \frac{-2z}{\lambda}, \tag{2.8}$$

where $z$ is the distance between the tip and the sample, $\lambda = \hbar/(2m\phi)^{1/2}$, and $\phi$ is the work function of the material. A typical work function of metal $o = 4$ eV gives $\lambda \approx 1$ Å. This means that the tunnel current is highly sensitive to the separation. An ideal resolution of STM for the z-direction is less than 0.1 Å.

Next, we describe the principle of scanning tunneling spectroscopy (STS)(see Fig.2.2.2). The concept is similar to conventional tunneling spectroscopy. When an STM measurement is being done, the feedback loop is made open only a short time, during which the bias voltage is ramped. The resulting current includes information about the density of states of the sample surface. By assuming that the tunnel probability between the sample and the tip is constant regardless of the bias voltage $V$, the tunnel current $I$ and the derivative $dI/dV$ at $T = 0$ are



written by

$$I \propto \int_{E_F}^{E_F+eV} \rho(\mathbf{r}, E)dE, \tag{2.9}$$

$$\frac{dI}{dV} \propto \rho(\mathbf{r}, E_F + eV), \tag{2.10}$$

where $\rho(\mathbf{r}, E)$ is the local density of states at point $\mathbf{r}$. Thus, the derivative directly gives the density of states of the sample surface. The main advantage of STS is that a *local* density of states of the surface can be obtained, while the conventional tunneling spectroscopy only detects a density of states *averaged* over a wide area.

There are so many applications of STM that we cannot treat all of them in this thesis. We will take only experiments on the charging effect in Section 2.3.3. For review, see Ref.[17] for example.

## 2.3 Single Electron Tunneling and Coulomb blockade

In late 1960's Zeller and Giaever [18] and Lamb and Jaklevic [19] first studied charging effects on single electron tunneling using a system of small metal droplets sandwiched between two oxidized metal electrodes. Now the advance of submicron fabrication technique in recent years has brought about many new findings about charging effects.

### 2.3.1 Basic Concepts

Let us consider a small tunnel junction with an area smaller than $10^{-2}$ $\mu$m$^2$(see Fig.2.3.1). The capacitance $C$ of such a junction is as small as $10^{-16}$ F, and the charging energy $e^2/2C$ associated with a transfer of *one* electron through the junction corresponds to 1 K in temperature. This means that the charging energy strongly influences the transport properties at low temperature. When

the charge $Q$ stored in the junction changes by $e$, the change in charging energy amounts to

$$(Q \pm e)^2/2C - Q^2/2C = e(\pm 2Q + e)/2C. \tag{2.11}$$

If $|Q| < e/2$, the charging energy increases by a tunnel event; hence, an electron cannot transfer through the junction (see Fig2.3.2). This is called the Coulomb blockade of tunneling.

To observe the Coulomb blockade, the resistance of the junction must be larger than what is called the quantum resistance $R_Q \equiv h/4e^2$. If this condition is not satisfied, electrons do not localize in one of the electrodes and the concept of one by one electron tunneling is no longer justified. We will discuss this charge fluctuation effect again in Section 2.3.4.

Let us consider a junction biased by a current source. The junction is gradually charged up by constant electron flow till $Q = e/2$. When $Q > e/2$, an electron, with certain probability, tunnels the junction and the charge $Q$ changes to $Q - e$, because it is no more Coulomb-blocked. The repetition of this process results in a correlation of consequent tunneling events in time, namely single-electron-tunneling (SET) oscillation. For more extensive reviews, see Ref.[3].

### 2.3.2 Coulomb Blockade in Double Junction Systems

A single junction system is desirable to investigate charging effects, for it is simple and easy to analyze. However, it is difficult to realize it in an experiment because the environment, namely an outer circuit attached to it, strongly affects the properties of a single junction. In contrast, in a multi-junction the inside electrodes are decoupled from the environment by the high tunnel resistances and the charging effects can be easily seen. For this reason, multi-junction systems have mainly been used experimentally so far.

Let us consider the double junction system with capacitances $C_1$ and $C_2$, and voltage supply $V$ (Fig.2.3.3). When the resistances $R_1$ and $R_2$ are much greater than the quantum resistance $R_Q$, the system is described in a semi-classical way.



The energy diagram of the system is schematically shown in Fig.2.3.4, where $C \equiv C_1 + C_2$. If an electron transfers from the left electrode to the middle, the Fermi level shifts up by the charging energy $e^2/2C$ and a charge of $eC_2/C$ passes through the voltage supply. The increase in charging energy must be equal to the work done by the voltage supply, $eVC_2/C$. Hence, the threshold voltage for current flow is found to be $V = e/2C_2$ from the relation $e^2/2C = eVC_2/C$. In the same way, an electron transfer from the middle to the left requires a threshold voltage $V = e/2C_1$. Thus, the threshold for current flow from the left to the right electrode is the smaller of $e/2C_1$ and $e/2C_2$. An electron tunneling is prohibited below this voltage (the Coulomb blockade).

When the junction is asymmetric ($R_1 > R_2, C_1 > C_2$), the current through the system is limited by the higher resistance $R_1$. A seldom electron transfer through the junction 1 is quickly followed by that through the junction 2, keeping the number of electrons $n$ on the middle electrode integer. With increasing voltage across the junctions, $n$ increases stepwise and correspondingly the voltage across the junction 1 $\Delta V = (VC_1 + ne)/C$ and the current $\Delta V/R_1$ increase stepwise [4]. The resulting step-like $I - V$ characteristic is the called Coulomb staircase, which has been experimentally observed [20]. The $I - V$ characteristics of double junctions is obtained from the so-called orthodox theory. In this theory, ensemble-averaged dynamics for the system is obtained from the master equation for $\rho(N, V, t)$, the probability that there are $N$ extra electrons on the middle electrode at time $t$ with applied voltage $V$. The number of electrons is treated as a classical variable, and the master equation describes stochastic process of electron transfers. Their solution is given by Amman *et al.* [21]. In Fig.2.3.5 we show their solution for different parameters. A clear Coulomb staircase shows up for $R_1 > R_2$ and $C_1 > C_2$, while only a slight staircase is seen for $R_1 > R_2, C_1 < C_2$ or for $R_1 = R_2, C_1 = C_2$.

In real junctions, the Fermi levels of the electrodes are different in general even when no bias voltage is applied, owing to the difference of work functions of the electrode metals. To compensate the difference of the Fermi levels, so-called fractional charge is stored on the middle electrode. The fractional charge $Q_f$

shifts the threshold voltage by $Q_f/C_1$ and, when $Q_f = e/2$, completely washes out the Coulomb blockade. One can also induce it by artificially attaching a gate to the middle electrode for the purpose of controlling the current flow through the junctions. This device is called an SET transistor [20].

### 2.3.3 Experiments Using STM

When a metal particle deposited on an oxidized metal substrate is probed with an STM tip, a double junction system is realized as illustrated in Fig.2.3.6 [4]. Such an experiment has the following advantages:

- The junction parameters, namely resistance and capacitance, can be easily changed by moving the tip.
- Extremely small capacitances ($\approx 10^{-18}$ F) can be obtained. This enables experiments at relatively high temperature (sometimes even at room temperature).

Bentum *et al.* first observed the Coulomb blockade using an STM [22]. They claimed that no particle was present between the tip and the substrate, and that they observed the Coulomb blockade with a single junction. However, a metallic impurity embedded in the oxide layer seems to have formed a double junction system in their experiment [23]. Willkins *et al.* [24] used a metal droplet deposited on a substrate and observed clear Coulomb staircases, which quantitatively agree with the theory by Mullen *et al.*. As for an experiment at room temperature, Schönenberger *et al.* first observed a clear Coulomb staircase [25]. Few groups have reported observing the sample surface with an STM in this kind of experiment [26], probably owing to feedback instability resulting from scanning over an oxidized surface. McGreer *et al.* used a superconducting particle as a middle electrode [27]. They showed that in an observed Coulomb staircase the voltage width of the step that crossed zero bias was larger than that of other steps. This is, they claimed, due to superconductivity of the particle and consistent with a theory by Mullen *et al.* [28]



### 2.3.4 Quantum Fluctuation Effect on Coulomb blockade

As mentioned earlier, when the resistance of the tunnel junction $R$ is smaller than the quantum resistance $R_Q$, the Coulomb blockade disappears. This can be explained as the following [29]. To transfer an electron from one electrode to the other, which are initially neutral, charging energy $e^2/2C$ is needed. However, if the energy-level width $\Delta E$ of this state related to the decay time $\tau$ is larger than the charging energy $e^2/2C$, an electron can occupy the state virtually so that no energy is needed to transfer an electron. This means that the Coulomb blockade does not appear. The uncertainty principle $\Delta \approx \hbar/\tau$ and $\tau = RC$, in this way, lead to $R > h/\pi e^2$ as a condition for observing the Coulomb blockade.

Brown and Šimánek calculated the dc zero-bias conductance of a single junction as a function of the junction conductance $R_N^{-1}$ and the temperature by use of functional-integral description [30]. They claimed that there is a precipitous transition from the Coulomb gap to the Ohmic behavior at $R \approx R_Q$ at low temperature. Their result is shown in Fig.2.3.7. Geerlig *et al.* [31] measured a series of resistances of multi-junctions and claimed that the temperature dependence are in good agreement with the theory by Brown and Šimánek. The dependence on the junction resistance, however, seems to change gradually contrary to the theory.

Although other theories and experiments have been carried out, it appears that the crossover behavior near $R_Q$ has not been understood yet. Further studies are needed to clarify this problem in terms of both experiment and theory.

# Chapter 3

# STM Design and Operation

Although many STM systems are commercially available these days, we have built our original STM instruments. This has allowed us to improve the system easily and use it in a versatile way. The STM consists of the three main parts: a mechanical component, electronics, and a personal computer(PC). For a review of STM instrumentation, see Ref.[32].

## 3.1 Mechanical Design

The mechanical component of the STM comprises the following parts.

- Tunneling and scanning assembly (STM head)
- Sample-tip approach mechanism
- Cryostat and vibration isolation

### 3.1.1 Head

Since a complex vibration isolation system cannot be incorporated into the STM cryostat, a high resonance frequency of the head is needed to realize a stable feedback operation. This requires the compact size and hardness of the head, which are crucial criteria for a low-temperature STM design. Compactness is also necessary because of the limited space in the cryostat. As is shown in





Fig.3.1.1(a), the head involves a scanner, a sample holder, and a tip. [1] The frame of the head is made of stainless steel because of its hardness.

#### Scanner

Figure 3.1.1(b) shows details of the scanner. The scanner is, in favor of its compact size, composed of four piezoelectric actuators, which are glued to one another with Stycast 2850. For a simultaneous motion of the scanner in the vertical (Z) and lateral(XY) directions, four different voltages are applied; (Vz-Vx, Vz+Vx) to one pair of actuators and (Vz-Vy, Vz+Vy) to the other. The voltage Vz moves the scanner in the vertical direction, while Vx or Vy bends it like a bimetal to make a lateral motion.

Piezoelectric actuators are accumulated types (TOKIN, NLA-1.4 $\times$ 3 $\times$ 9), which realize a large piezoelectric constant of 65 nm/V. Since the responce of piezoelectric actuator is highly reduced at low temperature while it is necessary to keep the size small, this large piezoelectric constant is advantageous for low temperature use. The voltage applied to the scanner is 110 V at maximum, which corresponds to a scanning range of 310 nm in the lateral direction and a stroke of 78 nm in the vertical direction at 4.2 K. The scanner is calibrated by observing a regular metal pattern fabricated with electron beam lithography.

#### Tip

A tip is one of the most important parts of the STM system, because reliability of STM experiments is highly dependent on a tip. For this reason, we used commercial STM tips (PtIr, mechanical etching, SEIKO ), although self-made STM tips, such as ones made by electrochemical etching, are widely used.

#### Sample Holder

[1] We are indebted to Dr.T.Hasegawa of Kitazawa group for the mechanical design.

To avoid creep or vibration, the sample must be tightly fixed to the sample holder when STM measurement is running. At the same time, it is desirable that one can easily remove or fix a sample. To meet these two demands, we have devised a rather simple sample holder that is shown in Fig.3.1.1(c). Mica sheets are inserted between the sample and the sample holder, so that electrical isolation between them may be kept good.

### 3.1.2 Sample-Tip Approach Mechanism

To carry out an STM measurement, the tip needs to be brought within about 2 nm from the sample surface without a contact of the tip and the sample. This requires much care about an approach mechanism.

Figure 3.1.2 shows the schematic diagram of the sample-tip approach mechanism that we adopted. The sample is brought in the proximity of the tip to about 15 $\mu$m during preparation. The stepping motor, which is driven by computer-generated pulses, rotates the rod that runs from the outside of the cryostat to the head. The rod rotates the screw in turn and moves it backward. This displacement is reduced by the lever by a ratio of 1/4, thus bringing the sample to the tip. Since one step of the stepping motor is $1/10^5$ of a rotation, and a pitch of the screw is 0.2 mm, the displacement per step is 0.5 nm, which is sufficiently small for our purpose.

Once a tunnel current between the tip and the sample is detected, the tip is drawn back to avoid a contact. Then, again, the tip is brought to the sample slowly by applying voltages to the scanner and expanding it, and finally a feedback tunnel current is obtained. When a measurement is being done, the rod is kept detached from the screw to prevent undesirable disturbances coming in through the rod.



### 3.1.3 Cryostat and Vibration Isolation

The cryostat includes a conventional Dewar vessel 42 mm in inner diameter and 750 mm in length. The STM head is directly immersed in liquid helium stored in the Dewar vessel, and temperature can be changed from 4.2 K to 1.6 K by pumping liquid helium.

We have not employed a full vibration isolation system because it is hard to do so as mentioned earlier. We only used is a widely adopted, simple air spring with an air compressor, on which the cryostat is placed. In contrast to this, when designing a low-temperature STM, one needs to pay more attention to noises arising in the cryostat. For example, helium bubbles induced by pumping produce large noise, making measurements impossible. We sometimes detected large noise that makes the feedback unstable even at 4.2 K or at temperatures below the $\lambda$ point. It appears that this is due to flows of liquid helium caused by thermal gradient.

## 3.2 Electronics Design

The electronic circuits of the STM are composed of three parts: current/voltage converter(i.e. preamplifier), main feedback circuits, and computer I/O.

### 3.2.1 Circuit Diagram

Figure 3.2.1 shows the circuit diagram of the STM system. A tunnel current caused by the bias voltage between the sample and the tip is converted into a voltage by the preamplifier, and then compared with the reference voltage. The difference between the two voltage values is low-pass filtered, amplified with the high voltage amplifier, and applied to the Z-scanner, which changes the height of the tip. The negative feedback loop keeps the tunnel current constant, resulting in a constant distance between the sample and the tip.

The scanning motion is produced by applying voltage ramps, which are

generated by the PC and high voltage amplifiers, to the X- and Y- scanners. The voltage applied to the Z-scanner is also put into the PC, and, when the X-Y scanning is performed, shown on the display monitor in the form of the sample surface corrugation. The bias voltage and the reference voltage determining the tunnel current value can be changed by the PC.

An STS procedure is as follows. First, the feedback loop is made open, and the bias voltage is ramped. The resultant change in the tunnel current is recorded in the PC memory, and finally the feedback loop is made closed again.

### 3.2.2 Preamplifier and Bias Supply

The preamplifier is the most important electronic component that determines the whole performance of the circuits. Since detected tunnel current is small, typically 100 pA, and easily affected by noise, it is demanded that the input-bias-current of the preamplifier be much smaller than the tunnel current and noise be as low as possible.

Figure 3.2.2(a) shows the circuit of the preamplifier. Using a resistance of 10 MΩ, a gain of $10^7$ V/A is obtained. The operational amplifier(OP-amp) in this circuit is an AD549(Analog Devise), which has sufficiently low input-bias-current(0.15 pA, typical). To reduce noise, the power of the preamplifier is supplied from two batteries.

Since the lead connecting the preamplifier and the sample is a long, high-impedance line, it is particularly affected by noise and a leakage current from this line must be sufficiently small. Parasitic capacitance of the lead should also be small because it tends to make the circuit unstable. For these reasons we have adopted a plain formalin-coated lead covered with a shielding stainless tube. In addition, terminals of the sample-preamplifier line are made of Teflon to reduce leakage current.

The bias voltage is generated by a 16-bit digital/analog converter(DAC), which is directly connected to the PC, to facilitate STS measurements. The bias voltage range can be selected from ±10 mV to ±10 V. For example, when



the range of ±1 V is selected, the resolution of the bias voltage is about 0.02 mV. These range and resolution are suitable for measuring both a superconducting energy gap and a Coulomb-blockade offset voltage for fine particles.

### 3.2.3 Main circuits

The output of the preamplifier is fed to the main feedback circuit, details of which are shown in Fig.3.2.2(b). It includes the following components.

#### First-stage amplifier

The difference of the input signal and the ground level is amplified with a gain of 10 to compensate the different ground levels of the preamplifier and the main circuit. It also plays a role of buffering the input signal that comes through a long coaxial cable.

#### Logarithmic amplifier

The signal is inverted if negative because the logarithmic amplifier needs a positive input regardless of the sign of the tunnel current. The logarithmic amplifier is a Log100(Burr Brown), which linearizes the exponential behavior of the tunnel current. This component has two advantages: the open-loop gain of the control system becomes independent of the sample-tip separation, and the difficulties associated with stabilizing a nonlinear system are avoided.

#### Comparator

The comparator compares the output of the logarithmic amplifier and a reference voltage that determines the tunnel current, and outputs the difference of the two.

#### Integrator

This component has a set of resistors ranging from 100 kΩ to 10 MΩ and a capacitor of 1.1 $\mu$C, resulting in a time constant $RC$ from 0.1 s to 10 s. For an open-loop gain $A$, a time constant of the integrator $\tau_i$, and a response time of the feedback system $\tau_f$, we get

$$\tau_f = \tau_i / A. \tag{3.1}$$

For example, typical values $A = 100$, $\tau_i = 0.1$ s provide $\tau_f = 1$ ms. Thus, the integrator determines the response time of the STM feedback system.

#### High-voltage amplifier

In the final stage, the feedback signal added to a DAC-generated offset voltage is put into the high-voltage amplifier with a gain of 20 and a output range of ±110 V. This high-voltage amplifier is not appropriate for a room-temperature measurement, for the gain of the feedback loop is too high because of the large sensitivity of the scanner at room temperature. For this purpose, an alternative amplifier with a gain of 2 and an output range of ±13 V is used.

### 3.2.4 Computer I/O

The bias voltage and the reference voltage for the tunnel current are generated by the PC and 16-bit DAC's. The X- and Y- voltages and the Z-offset voltage are also provided by the PC and DAC's. The tunnel current converted by the preamplifier and the Z-total voltage, which is the sum of the integrator output and the Z-offset voltage, are sent to the PC through analog-digital converters(ADC's).

A computer can be a great noise source because it has a number of digital IC's and fast CPU clock pulses. To protect the STM circuit from the PC noise, the ground of the PC and that of the STM circuit are isolated using photo-isolators.



## 3.3 Computer and Software

A PC-9801-RA(NEC) is used for the PC. The program that controls the whole STM system is written in the C-language, which is suitable for low-level control of a hardware. After an STM measurement, data stored in the disk can be processed with other software to make clear images or graphs.

# Chapter 4

# Experiments

## 4.1 Sample Preparation

We prepared the samples by thermally evaporating metals from a crucible in a vacuum chamber at a pressure of about $3 \times 10^{-6}$ Torr. First, Au or Ag was deposited on a substrate as a base layer. The thickness, monitored by a quartz oscillator thickness gauge, was about 600 Å. The base layer is thick enough that it forms a continuous film. Then a small amount of Al, 10 Å thick, was deposited on the base layer, and oxidized through exposure to pure oxygen at pressure of 0.1 Torr for 30 minutes. Al tends to make a continuous film instead of a granular one when thermally deposited and has few pin holes when oxidized. This nature of Al is adequate for a tunnel barrier. Last, a thin layer of Au, Ag, or In about 10 to 50 Å in mass thickness was deposited in order to form isolated particles. To ensure that the last layer became isolated particles instead of a continuous film, substrate temperature was raised if necessary.

We chose a silicon wafer or a freshly cleaved mica as the substrate. In particular, we used a cleaved mica to observe a sample surface. When a certain kind of metal such as Ag and Au is thermally deposited on a cleaved mica whose temperature is kept high(100 °C $\sim$ 200 °C), an extremely flat layer is obtained [33]. This makes it easy to distinguish the particles from the corrugation of the base layer when one takes a sample image using STM.

For experiments with superconducting particles, we used In for the last layer. Since In is relatively inert among the superconducting metals, it is advantageous for the use in STM experiments, which favors a clean metallic surface. In





addition, In easily forms isolated particles when thermally deposited, which is also adequate for our experiments. For normal-metal particles, we chose Au or Ag, also in consideration of their inertness.

Some of the samples thus fabricated were observed with an atomic force microscope(AFM) (TMX2000, Topometrix) to check the particle sizes. Figures 4.1.1(a)(b) show a typical AFM image of the base layer and that of a sample surface. After taken out from the evaporation chamber, the sample was immediately mounted on an STM head to avoid surface oxidization and contamination.

## 4.2 Measurements

After setting the sample, the STM head was inserted into a cryostat to measure a feedback current at room temperature. The sample and the measurement system were checked through this procedure. The cooling down of the STM head to the liquid nitrogen temperature should be done slowly because rapid decrease in temperature fatally damages the piezoelectric actuator. For this purpose, helium exchange gas was introduced in the inner Dewar, and the head was cooled down with liquid nitrogen stored in the outer Dewar. It took several hours for the temperature inside the Dewar to become that of liquid nitrogen. Measurements were carried out in liquid helium at temperatures ranging from 1.6 K to 4.2 K.

When the sample surface is scanned to take an image, an over-fast scan is undesirable because it causes the tip to contact with the sample, damaging both of them. A scanning time of 20 minutes was chosen to take an image of a 200 nm×200 nm area. Although this is relatively long compared to the usually adopted value, temperature stability in liquid helium excludes a possible thermal drift due to the long scanning time.

To take an $I-V$ characteristics at a certain point of the sample, we used the conventional STS method. The feedback loop was made open for 0.5 second, during which the bias voltage was ramped, and made closed again to stabilize

the current. This cycle was repeated 80 times and averaged to reduce high frequency noise. The resultant current was numerically differentiated to get a conductance-voltage characteristics. We also measured $I-V$ characteristics for different heights of the STM tip to the sample. For an experiment with normal-metal particles, the displacement of the tip was controlled, while for that with superconducting particles, the feedback current was controlled.

# Chapter 5

# Results and Discussion

## 5.1 Normal-Metal Fine Particles

### 5.1.1 Coulomb Blockade and the Coulomb Staircase

In this section, we show our results in detail to demonstrate the capability of our STM and samples for reproducing past experiments. We have routinely observed $I-V$ curves showing the Coulomb blockade for many samples. Figure 5.1.1 and Figure 5.1.2. show typical Coulomb-blockade $I-V$ characteristics. In Fig.5.1.1, one can see current suppression region around zero bias and almost linear increase above the threshold voltage. The overall shape is similar to the $I-V$ curve for symmetric case in Fig.2.3.5, though the increase in current at the threshold is slightly slow. In contrast, Fig.5.1.2 shows a clear step-like curve with equidistant width, namely the Coulomb staircase. As explained in Section 2.3.2, the Coulomb staircase appears when the system is asymmetric. The shift of about 50 mV in bias voltage, which is often observed in STM experiments, is attributed to a fractional charge in the particle. It is said that a charge trapped in an impurity in the oxide layer plays a role of the gate in an SET transistor and induces the fractional charge [24].

Let us estimate a parameter for the Coulomb staircase in Fig.5.1.2. When $C_1$ is the larger capacitance of the two, the step width $\Delta V$ of the Coulomb staircase equals to $e/C_1$. From the figure, $\Delta V = 320$ mV gives $C_1 = 0.51$ aF (aF $= 10^{-18}$ F). We identify the capacitance of the substrate-particle junction as $C_1$, because this junction contains the aluminum oxide layer with a large dielectric constant

$\epsilon_r(\approx 10)$ and has a larger junction area than the other one. For the particle diameter $2r$, the thickness of oxide layer $d$, we obtain the following relation by assuming a parallel-plate capacitor model (Fig.5.1.3):

$$C_1 = \epsilon_0 \epsilon_r \pi r^2 / d. \tag{5.1}$$

This relation gives $2r = 29$ Å, which is reasonable for the mass thickness 10 Å of the last deposited layer.

Figure 5.1.4 shows the Coulomb-blockade $I-V$ characteristics measured at room temperature. The charging energy is estimated to be 200 meV from the offset voltage. This energy corresponds to $2.4 \times 10^3$ K, which is much larger than the room temperature. This shows that the Coulomb blockade can be seen even at room temperature if the charging energy is large enough.

The results in this section are in accordance with previous experiments, such as that by Willkins *et al.* [24].

### 5.1.2 Surface Images

Figure 5.1.5 shows two STM images of the same surface area of a sample Ag30Å/$Al_2O_3$10Å/Ag550Å/mica. As is seen from them, reproducibility of the image is fairly good. The area of one "island" is about 30 nm× 50 nm, which agrees well with the AFM images (Fig.4.1.1(b)) of the same sample. Apparent slight corrugation is due to low-pass filtering of software process for reducing noise. Between the two scans, $I-V$ curves were measured at several points by STS. Coulomb-blockade features were obtained at points A, C, and E, but not in many other points. The offset voltage of these $I-V$ curves are 40 mV, 10 mV, and 12 mV, respectively, which correspond to particle diameters of 59 Å ,120 Å and 110 Å. These diameters are rather different from the size of islands mentioned above. The discrepancy shows that the observed Coulomb blockade features are not of the "islands" that are visible in Fig.5.1.5, but of smaller particles. We believe that Au "islands" covers a large part of the substrate and are connected to one another in spite of its appearance.



For a large structure such as this case, it is difficult to know the precise structure of the sample surface using STM or AFM from the following reasons. First, an STM or AFM image is, in general, a convolution of surface structures of both the tip and the sample. In other words, the image reflects the structure of the tip as well as that of the sample. Moreover, the STM tip is often too dull to probe valleys of the surface. This makes particle images apparently in contact with one another and larger than the real sizes.

In contrast to the above case, we were not able to get clear and reproducible images when the Coulomb blockade was easily observed at many points. Such a sample is expected to contain many isolated particles, so that the oxide layer can be probed directly with the STM tip. From the comparison of the two types of samples, we conclude that contacts of the tip with the oxide layer make the STM feedback unstable and consequently prevent an image to be gained. To gain a reproducible image, the sample should be prepared in such a way that topmost layer particles covers almost all area of the surface, as pointed out by Amman *et al.* [26].

### 5.1.3 Smearing of the Coulomb Blockade Caused by Sample-Tip Approach

When biased by a voltage source, a single junction with small capacitance does not exhibit charging effect even if the junction resistance $R$ is much higher than the quantum resistance $R_Q$. This is because, if an electron tunnels the junction, the voltage source quickly responds to the change to keep the charge in the junction constant. Hence, it leads to no increase in charging energy, resulting in no Coulomb blockade. [1] Therefore, it is expected, in our experiment, that the Coulomb blockade disappears when the STM tip approaches the particle and the junction resistance between them becomes zero; *i.e.*, the system turns

[1] This is related to the difficulty of observing the charging effect using current-biased single junction. Parasitic capacitance of the leads, which is much larger than the junction capacitance, plays a role of voltage source and washes out the charging effect in real experiments.

from double junctions into a single junction. We can put this in another way. That is, electrons in the middle electrode are well localized when the resistances of the adjacent junctions are sufficiently high. However, they come to fluctuate as one of resistances becomes smaller than a certain value, and consequently the Coulomb blockade disappears. The critical resistance for vanishment of the Coulomb blockade is expected to be about $R_Q (= 6.5\ \mathrm{k}\Omega)$ from the argument in Section 2.3.4.

Figure 5.1.6 shows a typical result of such an experiment. We moved the tip to the sample by 9 Å after obtaining one $I-V$ characteristics and repeated this process five times. The sequence of the measurements is shown by the numbers (1)-(5). It is seen that the Coulomb staircase was gradually smeared as the tip approached the particle and finally changed to a nearly Ohmic behavior. In this measurement the total shift of the STM tip was 36 Å. Although the dependence of the particle-tip resistance on the separation may be weak, we expect that the resistance varied to a considerable extent. Hence, the change of $I-V$ characteristics indicates that the Coulomb blockade in the double-junction system is slowly lifted as one of the resistances of the junctions becomes smaller. The critical resistance for lifting may be around $R_Q$, but it is not well defined. In the figure, the asymptotic resistance in the high-bias region is almost constant ($\approx 3\ \mathrm{M}\Omega$). Since it nearly equals to the higher base-particle resistance, this shows that the change of $I-V$ characteristics was really induced by the variation of the tip-particle resistance.

Amman *et al.* first observed smearing of the Coulomb staircase using an STM [26], but they mentioned it only briefly. We went further into detailed observation of smearing process of the Coulomb staircase. Our result indicates that STM is capable of studying the crossover between the Coulomb-blockade regime and the Ohmic regime. With detailed information about the tip height and a decay length of the wave function of the surface state, we could determine the behavior in this region more precisely.



## 5.2 Superconducting Fine Particles

### 5.2.1 Preliminary Experiment on a Superconducting Thin Film

As a preliminary experiment, we measured the energy spectrum of a thin In film with 3000 Å thickness by STS at 1.6 K. Figure 5.2.1 shows its typical result. The dip around zero bias voltage and the two peaks adjacent to it are due to superconducting energy gap. However, the spacing between the two peaks $2\Delta_{p-p} (= 2.4$ meV) is quite larger than the energy gap $2\Delta (= 1.00$ meV at 1.6 K) of In. (To determine the peak spacing precisely, we used the intersections of $d^2I/d^2V - V$ curve and the line $d^2I/d^2V = 0$.) For the BCS-like superconductor, the peak spacing $2\Delta_{p-p}$ in the spectrum should be equal to its superconducting energy gap $2\Delta$. In addition, the decrease in conductance around zero bias is not so sharp as expected from the BCS theory. These features of the spectrum of a superconductor are often seen in other STS measurements [34].

The enhancement and smearing of energy gap are explained by considering the life time of quasi particles [35]. If the life time of quasi particle $\tau_q$ is finite, the density of states $\rho(E)$ of a superconductor is written by

$$\rho(E) = Re\left[\frac{E + i\Gamma_q}{\sqrt{(E + i\Gamma_q)^2 - \Delta^2}}\right] \tag{5.2}$$

where $\Gamma_q = \hbar/\tau_q$ is an energy width associated with the life time. and E is the energy measured from the Fermi level. By taking into account the effect of temperature, we fit the data to Eq.(5.2) to obtain $\Delta = 0.65$ meV and $\Gamma_q = 0.38$ meV. We note that the observed peak spacing $2\Delta_{p-p}$ and the real energy gap $2\Delta$ must be distinguished.

Although the fitting is excellent, some disagreement remains between the energy gap determined by the experiment ($\Delta = 0.65$ meV at 1.6 K) and that of a bulk ($\Delta = 0.50$ meV at 1.6 K). It is well known that the transition temperature ($T_c$) of a superconducting film could be higher than that of a bulk,

probably owing to a difference in the electron-phonon coupling . The residual enhancement of the energy gap in this experiment may be related to the increase in $T_c$. From the averaged value of the same experiments, we obtained $\Delta = 0.70$ meV as an energy gap of a superconducting film at 1.6 K, which gives $\Delta = 0.74$ meV at 0 K. We will use this value later.

For an origin of the finite life time of quasi particles, large current densities inherent to STM and/or surface contamination are possible [34]. No change of the spectra, however, with an increase in current from 100 pA to 10 nA excludes the origin of high current density. On the other hand, a crash of the tip into the sample sometimes induces a clearer energy gap. Hence, we believe that surface contamination plays an important role for this non-ideal BCS-like behavior.

### 5.2.2 Transition from the Coulomb Gap to the Superconducting Energy Gap

As seen in the previous section, the Coulomb blockade disappears when the STM tip approaches the particle and the resistance of the tip-particle junction gets small enough so that fluctuation of the charge on the particle becomes large. Then what will happen if the particle is superconducting ? When the particle is as small as 100 Å, the Coulomb-blockade offset voltage is larger than superconducting energy gap, of the order of 1 mV. Hence, it is difficult to see superconducting energy gap in the larger Coulomb-blockade structure. However, superconducting energy gap is expected to appear after the Coulomb blockade will vanish with approach of the tip to the particle.

Figure 5.2.2 shows a typical AFM image of the sample used in this experiment. The topmost layer is made of isolated In particles. We did not take an image with the STM by the reason discussed in Section 5.1.2. Figure 5.2.3(a) shows two $I - V$ characteristics for different distances between the tip and the particle. First, we obtained a clear Coulomb staircase (curve(1)). The current suppression region 13 mV in width around zero bias voltage shows that a particle about 150 Å in diameter was present under the tip. Then we moved the



tip closer to the particle (curve(2)). It is seen that the staircase was smeared and the zero bias conductance changed to a finite value. Figure 5.2.3(b) shows a $dI/dV - V$ curve for the case (2). The dip around zero bias voltage and the two peaks adjacent to it are characteristics of superconducting energy gap. The spacing between the two peaks $2\Delta_{p-p}$ in the spectrum is 2.6 meV. The shape of the spectrum and the peak spacing $2\Delta_{p-p}$ almost equal to those of the thin In film shown in Fig.5.2.1.

As expected, we found that superconducting energy gap appears when the Coulomb blockade disappeared. This phenomenon is interesting from the following two points of view.

1. It is a sort of transition from the Coulomb-blockade-dominating phase to the superconductivity-dominating phase.

2. We are capable of spectroscopy of a single superconducting fine particle using this technique.

Although many experiments on superconducting fine particles have been carried out by NMR [11][13], their samples are all ensembles of small particles and the measured quantity is not energy spectrum, but such as the Knight shift and spin-lattice relaxation time. Zeller and Giaever determined the energy gap of superconducting fine particles by means of tunneling spectroscopy [14], but they also used samples of ensembles of particles and could not obtain energy spectrum. Mcgreer *et al.* observed the effect of superconductivity of a single particle on the Coulomb staircase [27], but this is not an observation of energy spectrum. The present experiment is the first to carry out spectroscopy of a single particle.

### 5.2.3 Particle-Size Dependence

We have estimated the size of a particle from the Coulomb-blockade offset voltage before its vanishment using the relation of Eq.(5.1). This estimation is more reliable than that from an STM or AFM particle image, which tends to

give a larger particle size than the real diameter as discussed in Section 5.1.2. In Fig.5.2.4 we plot the peak spacing $2\Delta_{p-p}$ versus the particle diameter $2r$. As seen from the graph, the peak spacing slightly increases with a decrease in diameter from 250 Å to 50 Å. This is contrary to the expected behavior that superconductivity should be suppressed as the particle size decreases, because a larger peak spacing means a larger energy gap in general.

Let us consider the reason why the peak spacing $2\Delta_{p-p}$ increases with a decrease in size. As described in Section 2.1.2, the order parameter thermally fluctuates when a particle is small enough that its superconducting condensation energy is comparable to the temperature. Sone calculated the density of states of a superconducting fine particle in the dirty limit and at temperatures with relatively wide range [36]. According to his theory, the fluctuation reduces the life time of Cooper pairs $\tau_s$ and, as a result, smears the otherwise sharp density of states. In addition, it broadens energy gap $\Delta$ effectively compared to that given by the BCS theory. The enhancement of the peak spacing originates from both smearing and increase in energy gap. The density of states $\rho(E)$ subject to fluctuation is written by

$$\rho(E) = Re\left[\frac{E + i\Gamma_s}{\sqrt{(E + i\Gamma_s)^2 - \Delta^2}}\right], \tag{5.3}$$

where $\Gamma_s = \hbar/\tau_s$ is an energy width associated with the life time, and $E$ is the energy measured from the Fermi level. Figure 5.2.5 shows the density of states for $\bar{\delta} = 0.1, 1.0$. The enhancement of energy gap is one of the origins of the anomalously long spin-lattice relaxation time measured by Kobayashi *et al.* [13] (Fig.5.2.6); it increases faster than the BCS prediction below $T_c$. Since the spin-lattice relaxation time below $T_c$ scales to $exp(\Delta/k_BT)$, this fast rise is attributed to a larger energy gap than that from the BCS theory. [2]

We calculated the spacing $2\Delta_{p-p}$ for the present experiment using Eq.(5.3). From Ref.[36], one can obtain $\Delta/\Delta(0)$ and $\Gamma_s/\Delta(0)$ as functions of $T$ for

[2]The other origin of the long relaxation time is the finite energy levels in the particle [37].



$\bar{\delta} = 0.1, 1.0, 3.0$, which correspond to $2r$ =170 Å, 78 Å, 54 Å, respectively for In particles. Here, $\Delta(0)$ is the energy gap of the material at $T = 0$ K. We determined $\Delta$ and $\Gamma_s$ by choosing $\Delta(0) = 0.74$ meV from the fitting of thin films. In addition, we took into account the effect of the finite life time of quasi particles by replacing $\Gamma_s$ with $\Gamma_s + \Gamma_q$. This replacement seems appropriate because Eq.(5.3) has the same form as Eq.(5.2). We assumed that $\Delta(0)$ and $\Gamma_q$ are independent of the particle diameter. The result is plotted in Fig.5.2.4 along with the experimental data. Qualitative agreement with the theory and the experiment suggests that the enhancement of the peak spacing is due to fluctuation.

Aside from the fluctuation effect, there have been studies on increase in $T_c$ of a superconducting fine particle so far [15]. Increase in $T_c$ and associated enhancement of energy gap may explain our experimental result. In the next section, we will compare the fluctuation effect with the increase in $T_c$ to discuss the origin of the gap enhancement.

### 5.2.4 Temperature Dependence

Figures 5.2.7(a)(b) show the temperature dependence of the spectrum of an In particle 160 Å in diameter and that of an In film 3000 Å in thickness. From bottom to top, temperature was varied as T=1.6 K, 2.2 K, 2.7 K, and 3.1 K. For a fine particle, we observed at 1.6 K a gap structure with $2\Delta_{p-p}$=2.5 meV, similar to Fig.5.2.3(b). When temperature increased to 2.2 K and 2.7 K, the two peaks seen at 1.6 K disappeared and the gap structure was smeared. Last, the dip around zero bias voltage disappeared at 3.1 K. If the dip was due to the Coulomb blockade, it would not disappear around these temperatures, because a Coulomb gap (2.5 meV) is much higher than the temperature. Considering that the transition temperature of In is 3.4 K, the dip structure arises from superconductivity. However, the change of the spectrum of a fine particle is rather different from that of a thin film. For the thin film, the two peaks characterizing superconducting energy gap was maintained until the gap disappeared at 3.1

K. We believe that the difference between the two temperature dependences can be attributed to fluctuation of the order parameter in a fine particle. It is probable that fluctuation smoothes out the superconducting gap structure, which is characterized by the two peaks near zero bias. Although this argument is in accordance with the enhancement of the peak spacing $2\Delta_{p-p}$ described in the above section, it does not exclude the possibility of increase in $T_C$ in a small particle. Indeed, some disagreement between the experiment and the fluctuation theory may be ascribed to this effect.

The shapes of the spectrum of the particle at 2.2 K and 2.7 K are much different from that calculated from the theory of Sone (see Fig.5.2.5). This is not astonishing because, although Sone's theory includes a variety of effects, it assumes a rather simple form Eq.(5.3) with only two parameters as the density of states. We stress that this unexpected shape of energy gap has been clarified by spectroscopy of a single fine particle.

Finally, we briefly mention possible other effects in our experiment. In the range of particle size less than 100 Å in diameter, the Kubo effect is expected to be important. However, low tunneling resistance of the junction between the tip and the particle will make short the life time of electrons in the particle and destroy the discrete energy levels. Consequently, the Kubo effect will not appear. The interaction between electrons in the particle and those in the tip may cause another effect, such as the Andreev reflection [38]. A junction made of a normal metal and a superconductor exhibits increase in current by a factor of two below the bias voltage equal to the superconducting energy gap. However, as far as our results, it did not occur. For the Andreev reflection to be observed, the two metals should be in good electric constant. We believe that thin oxide layer that covers the In particle separates it from the STM tip, preventing the effect from taking place.

# Chapter 6

# Conclusion

We have investigated the Coulomb blockade of tunneling in a small double junction system using STM/STS and a normal-metal fine particle on an oxidized metal substrate. The following results were obtained in this experiment.

- We observed clear $I-V$ characteristics showing the Coulomb blockade. In particular, the Coulomb staircase was routinely observed.
- We took a surface image of a sample that showed Coulomb-blockade features. The condition for surface imaging was found to be that metal particles covers almost entire region of the surface, preventing contacts of the STM tip to the oxide layer.
- The Coulomb staircase is smeared gradually and eventually disappeared as the STM tip approaches the particle. This indicates that the critical resistance for the transition from the Coulomb-blockade regime to the Ohmic regime is not well defined.

We have also studied superconducting fine particles by STS. The results are summarized as follows.

- Energy gap of superconducting thin film measured by STS was broadened and smeared. This is due to finite life time of quasi particles.
- For a fine particle, superconducting energy gap showed up after the vanishement of the Coulomb blockade caused by tip approach. This permitted spectroscopy of a single superconducting fine particle.

- We measured the dependence of the peak spacing in the spectrum of a superconducting fine particle on its diameter. The peak spacing increases with a decrease in particle diameter from 250 Å to 50 Å. This dependence qualitatively agrees with the theory by Sone, which considers superconducting fluctuation.

- We measured changes of the spectrum of a fine particle at temperatures ranging from 1.6 K to 3.1 K. The superconducting gap structure characterized by the two peaks near zero bias was smeared before the gap disappeared, in contrast the case of a thin film. This can be attributed to fluctuation of the order parameter in a fine particle.

## Acknowledgment

I would like to gratefully acknowledge Prof. S. Kobayashi for giving me this theme, and for having encouraged me throughout this work. I also express my gratitude to him for proofreading the manuscript. I wish to thank Prof. S. Katumoto for his great help in building the STM used in this experiment. Dr. R. Yagi is also acknowledged for fruitful advices and discussions. I am indebted to Prof. S. Ikehata and Prof. Y. Ootuka for valuable advices and encouragement. Technical support of Mr. S. Ootsuka was also precious. Finally, I am grateful to all members of Kobayashi-Ikehata-Ootsuka group for their encouragement throughout.

# Bibliography

[1] R. Kubo, J. Phys. Soc. Jpn. **17**, 975 (1962), Electronic Properties of Metallic Fine Particles. I.

[2] M. Tinkham, *Introduction to Superconductivity*, McGrow-Hill (1975).

[3] D. V. Averin and K. K. Likharev, in *Mesoscopic Phenomena in Solids*, edited by B. L. Altshuler, P. A. Lee, and R. A. Webb ( North Holland, 1991).

[4] K. Mullen, E. Ben-Jacob, R. C. Jaklevic, and Z. Schuss, Phys. Rev. **B37**, 98 (1988), $I-V$ characteristics of ultrasmall-capacitance normal tunnel junctions.

[5] L. P. Gor'kov and G. M. Eliashberg, Sov. Phys. -JETP**21**, 940 (1965), MINUTE METALLIC PARTICLES IN AN ELECTROMAGNETIC FIELD.

[6] M. L. Mehta, *Random Matrices and Statical Theory of Energy Levels*, Academic Press, New York (1967).

[7] R. Denton, B. Mühlschegel, and D. J. Scalapino, Phys. Rev. **B7**, 3589 (1973), Thermodynamic Properties of Electrons in Small Metal Particles.

[8] S. Kobayashi, T. Takahashi, and W. Sasaki, J. Phys. Soc. Jpn. **31**, 1442 (1971), Fine Particle Size Effect of Metallic Al.

[9] B. Mühlschegel, D. J. Scalapino, and R. Denton, Phys. Rev. **B6**, 1767 (1972), Thermodynamic Properties of Small Superconducting Particles.

[10] R. A. Buhrman and W. P. Halperin, Phys. Rev. Lett. **30**, 692 (1973), Fluctuation Diamagnetism in a "Zero-Dimentional" Superconductor.

[11] M. Ido, J. Phys. Soc. Jpn. **41**, 412 (1976), Fluctuation Effect on the Knight Shift of Superconducting Al Fine Particles.

[12] P. W. Anderson, J. Phys. Chem. Solids **11**, 26 (1959), THEORY OF DIRTY SUPERCONDUCTORS.

[13] S. Kobayashi, T. Takahashi, and W. Sasaki, J. Phys. Soc. Jpn. **36**, 714 (1974), NMR Properties of Superconducting Fine Particles: Al and Sn.

[14] H. R. Zeller and I. Giaever, Physica **55**, 173 (1971), SUPERCONDUCTIVITY IN VERY SMALL PARTICLES.

[15] R. H. Parmenter, Phys. Rev. **166**, 392 (1968), Size Effect in a Granular Superconductor.

[16] G. Binnig, H. Rohrer, Ch. Gerber and E. Weiebel, Phys. Rev. Lett. **50**, 120 (1983), 7×7 Reconstruction on Si(111) Resolved in Real Space.

[17] *Scanning Tunneling Microscopy*, edited by J. A. Stroscio and W. J. Kaiser (Academic Press, Inc., 1993).

[18] H. R. Zeller and I. Giaever, Phys. Rev. **181**, 789 (1969), Tunneling, Zero-Bias Anomalies, and Small Superconductors.

[19] J. Lamb and R. C. Jaklevic, Phys. Rev. Lett. **22**, 1371 (1969), CHARGE-QUANTIZATION STUDIES USING A TUNNEL CAPACITOR.

[20] T. A. Fulton and G. J. Dolan, Phys. Rev. Lett. **59**, 109 (1987), Observation of Single-Electron Charging Effects in Small Tunnel Junctions.

[21] M. Amman, R. Wilkins, E. Ben-Jacob, P. D. Maker, and R. C. Jaklevic, Phys. Rev. **B43**, 1146 (1991), Analytic solution for the current-voltage characteristics of two mesoscopic tunnel junctions coupled in series.



[22] P. J. M. van Bentum, H. van Kempen, L. E. C. van Leemput, and P. A. A. Teunissen, Phys. Rev. Lett. **60**, 369 (1988), Single-Electron Tunneling Observed with Point-Contact Tunnel Junctions.

[23] R. Wilkins, M. Amman, E. Ben-Jacob, and R. C. Jaklevic, Phys. Rev. **B42**, 8698 (1990), Single-electron and oxide-impurity effects in junctions formed by a cryogenic scanning tunneling mictroscope.

[24] R. Wilkins, E. Ben-Jacob, and R. C. Jaklevic, Phys. Rev. Lett. **63**, 801 (1989), Scanning-Tunneling-Microscope Observations of Coulomb Blockade and Oxide Polarization in Small Metal Droplets.

[25] C. Schönenberger, H. van Houten ,and H. C. Donkersloot, Europhys. Lett. **20**, 249 (1992), Single-Electron Tunneling Observed at Room Temperature by Scanning-Tunneling Microscopy.

[26] M. Amman, S. B. Field, and R. C. Jaklevic, Phys. Rev. **B48**, 12 104 (1993), Coulomb-blockade spectroscopy of gold particles imaged with scanning tunneling microscopy.

[27] K. A. McGreer, J. -C. Wan, N. Anand, and A. M. Goldman, Phys. Rev. **B39**, 12 260 (1989), Superconducting energy gap in Coulomb staircase tunneling structures.

[28] K. Mullen, E. Ben-Jacob, and S. Ruggiero, Phys. Rev. **B38**, 5150 (1988), Charging effects in coupled superconducting tunnel junctions and their implications for tunneling measurements of high-$Tc$ superconductors.

[29] S. Kobayashi, Solid State Physics **28**, 804 (1993) (in Japanese).

[30] R. Brown and E. Šimánek, Phys. Rev. **B34**, 2957 (1986);Phys. Rev. **B45**, 6069 (1992), Transition to Ohmic conduction in ultrasmall tunnel junctions.

[31] L. J. Geerlig, V. F. Andergg, C. A. van der Jeugd, J. Romijn, and J. E. Mooij, Europhys. Lett. **10**, 79 (1989), Influence of Dissipation on the Coulomb Blockade in Small Tunnel Junctions.

[32] *Scanning Tunneling Microscopy and Spectroscopy*, edited by D. A. Bonnel (VHC Publishers, 1993).

[33] K. Reichelt and H. O. Lutz, J. Cryst. Growth **10**, 103 (1971), HETRO-EPITAXIAL GROWTH OF VACUUM EVAPORATED SILVER AND GOLD.

[34] Ch. Renner, A. D. Kent, Ph. Niedermann, and Ø. Fischer, Phys. Rev. Lett. **67**, 1650 (1991), Scanning Tunneling Spectroscopy of a Vortex Core from the Clean to the Dirty Limit.

[35] R. C. Dynes, V. Narayanamurti, and J. P. Garno, Phys. Rev. Lett. **41**, 1509 (1978), Direct Measurement of Quasiparticle-Lifetime Broadening in a Strong-Coupled Superconductor.

[36] J. Sone, J. Low Temp. Phys. **23**, 699 (1976), Nuclear Magnetic Resonance in Small Superconducting Particles. I.

[37] K. Nomura, S. Kobayashi, and W. Sasaki, J. Phys. Soc. Jpn. **48**, 37 (1980), NMR study of Al Small Particle.

[38] A. F. Andreev, Sov. Phys. JETP **19**, 1228 (1964), THE THERMAL CONDUCTIVITY OF INTERMEDIATE STATE IN SUPERCONDUCTORS.

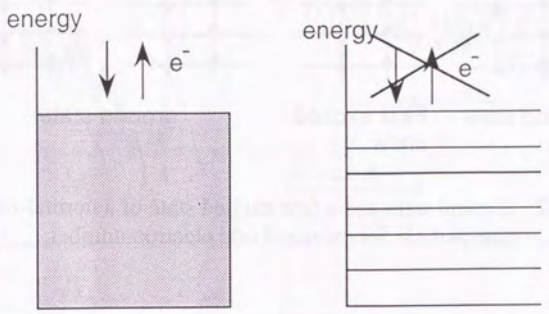


(a) bulk metal (b) fine particle

**Fig.2.1.1** Energy diagram of a bulk metal and a fine particle. (a) Energy spectrum is continuous and electron can freely leave and enters into it. (b) Energy spectrum is discrete. The number of electron in the particle is fixed.

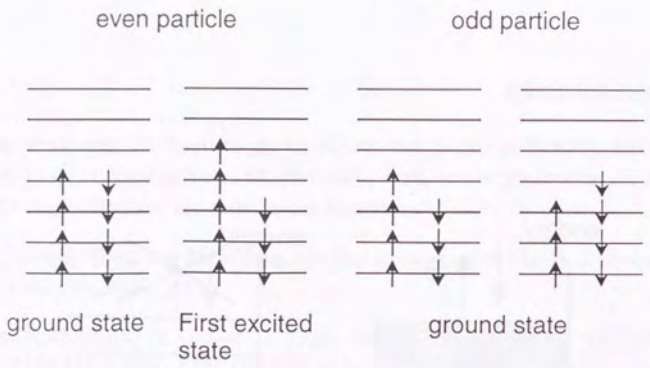


**Fig.2.1.2** Ground state and a first excited state of a normal-metal fine particle for even and odd electron number.

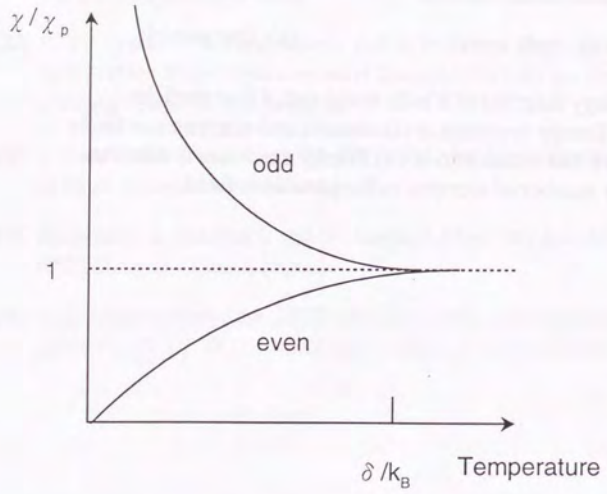


**Fig2.1.3** Spin susceptibility of a normal-metal fine paticle as a function of temperature.

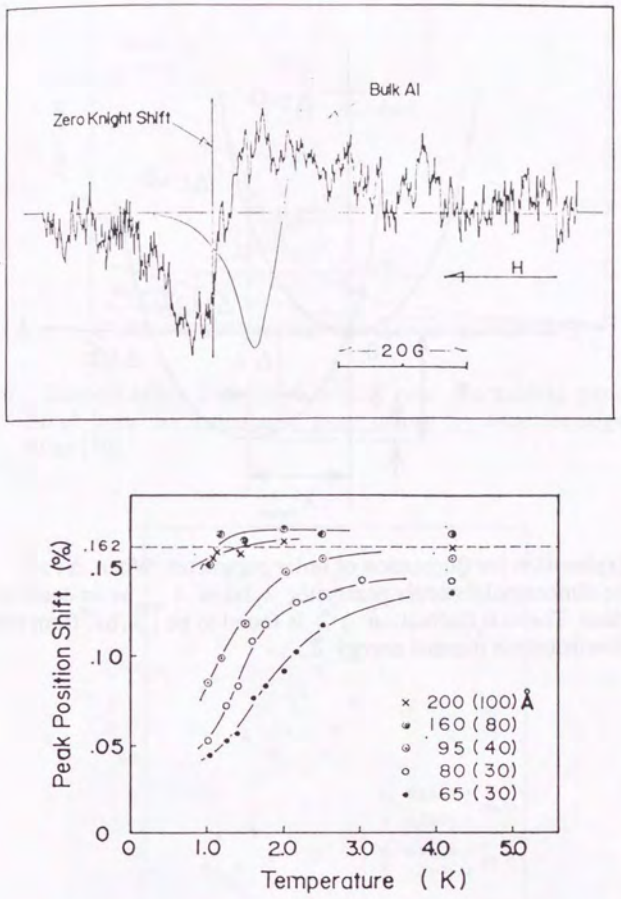


Fig.2.1.4 (a) NMR absorption differential line shape of Al particles with a mean diameter of 45 Å at 1.05K.
(b) Shift of NMR absorption peak position. The values in parentheses are the half value width of diameter distribution. The bulk Knight shift is given by a broken line. After [8].

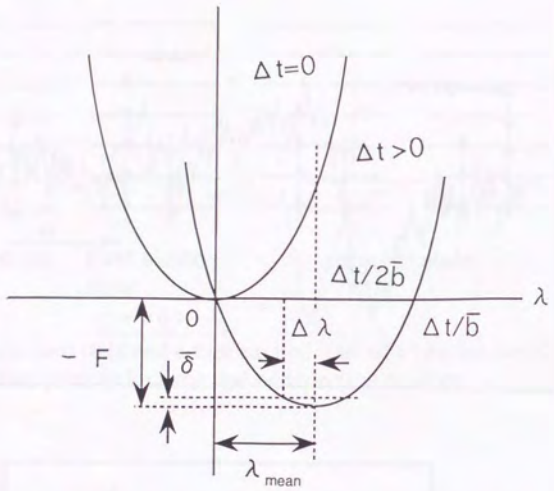


Fig.2.1.5 Explanation for fluctuation of order parameter. When $\Delta t > 0$, the dimensionless order parameter $\lambda$ takes $\lambda_{mean}$ as an equilibrium value. Thermal fluctuation $\Delta\lambda$ is found to be $(\delta/b)^{1/2}$ from the dimensionless thermal energy $\delta$.

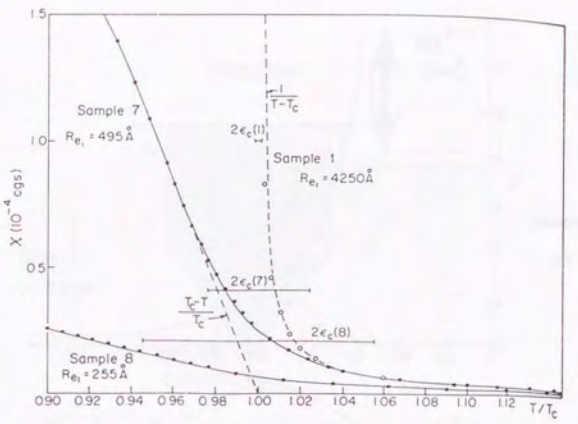


Fig.2.1.6 Susceptibility for three samples near the critical region. Solid lines are calculated from theory by Muehlschlegel et al. After [10].

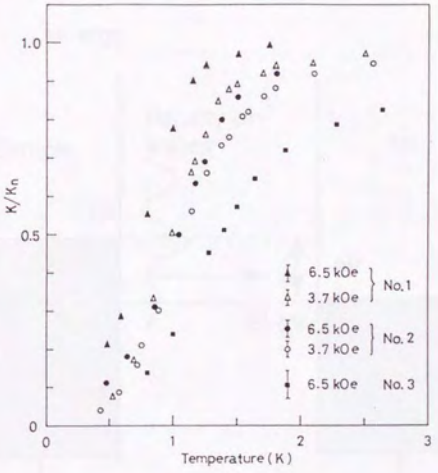


Fig.2.1.7 Temperature dependence of the Knight shift normalized to the value *Kn* in the normal state. After [11].

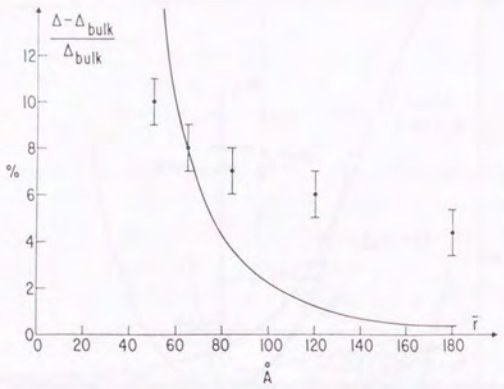


Fig.2.1.8 Size dependence of the energy gap. The solid line is calculated from Parmenter's formula based on the effect of $k$ quantizaion in the small particle. After [14].

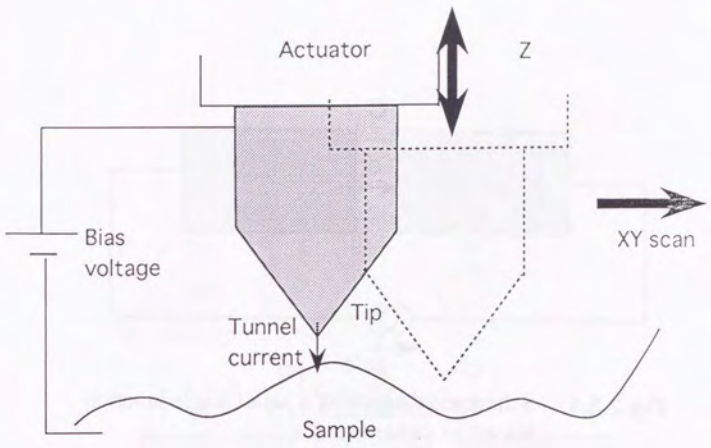


**Fig.2.2.1** Schematic diagram of the STM operation

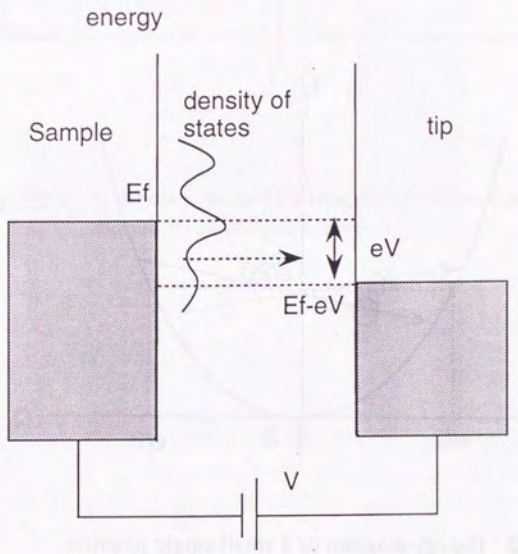


**Fig.2.2.2** Schematic diagram of STS

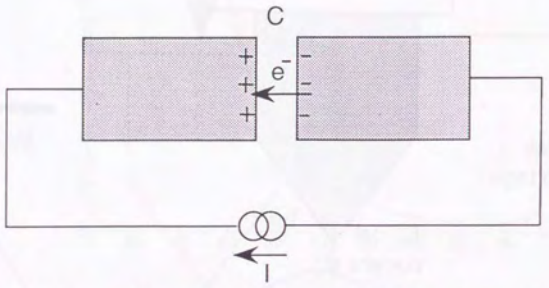


**Fig.2.3.1** Schematic diagram of a small single junction biased by current source

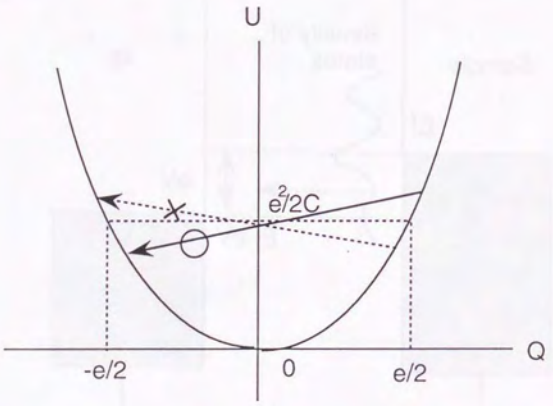


**Fig.2.3.2** Energy diagram of a small single junction. An electron tunneling that increases charging energy is prohibited .

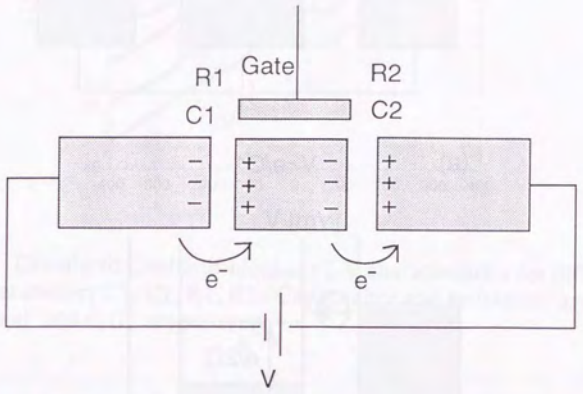


**Fig.2.3.3** Schematic view of a small double junction biased by a voltage source.

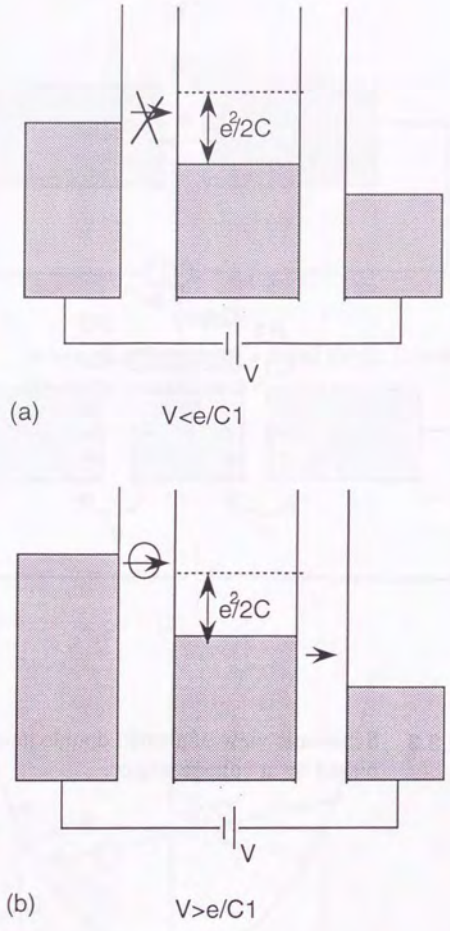


**Fig.2.3.4** Energy diagram of a double junction system biased by DC voltage. (a) An increase in charging energy prohibits electron tunneling .(b) The bias voltage is enough large for tunneling.

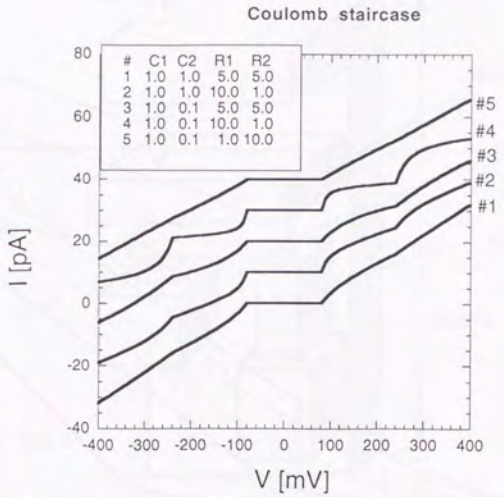


Fig.2.3.5 Calculated Coulomb-blockade I-V characteristics for different parameters C1, C2, R1, R2 . Capacitance and resistance are expressed in aF and GΩ, respectively.

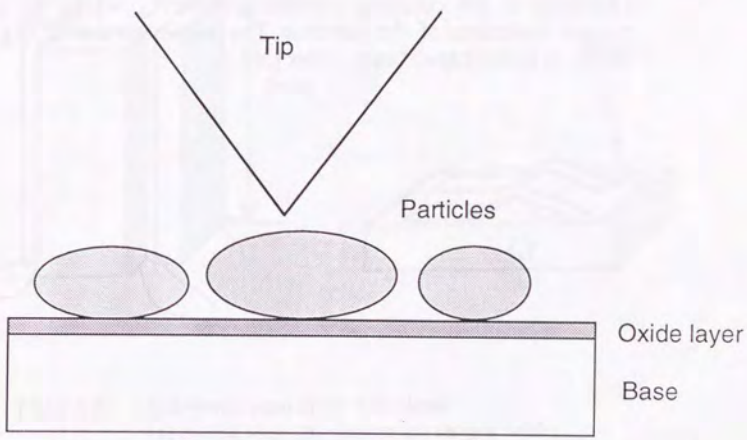


**Fig.2.3.6** Schematic View of a small double junction formed with a STM tip,a particle, and a base.

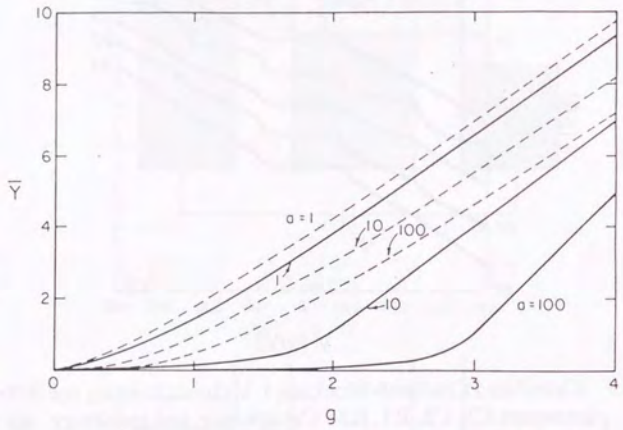


Fig.2.3.7 Dimensionless dc conductance $Y$ of a tunnel junction plotted as a functoin of the coupling constant $g=h/4e^2R_N$, where $R_N$ is the normal resistance of the junction. The parameter $a=e^2/2\pi^2k_BTC$, where $C$ is the capacitance. After [30].

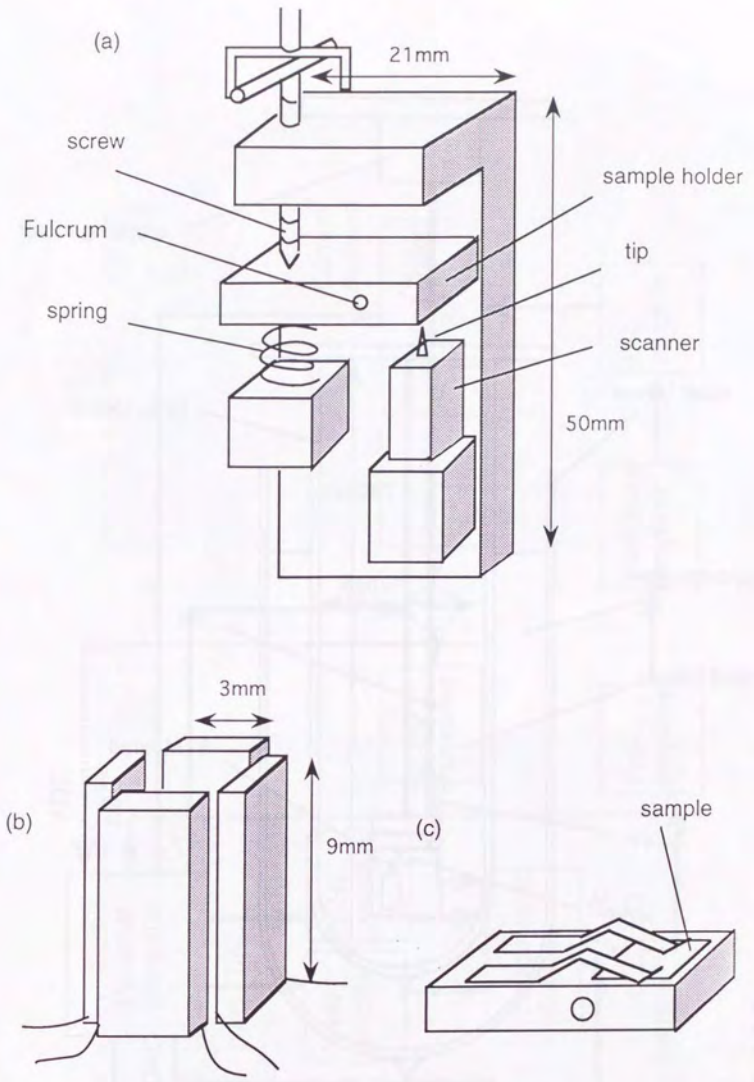


**Fig.3.1.1** Schematic view of the STM head.
(a) overall view (b) scanner (c) sample holder.

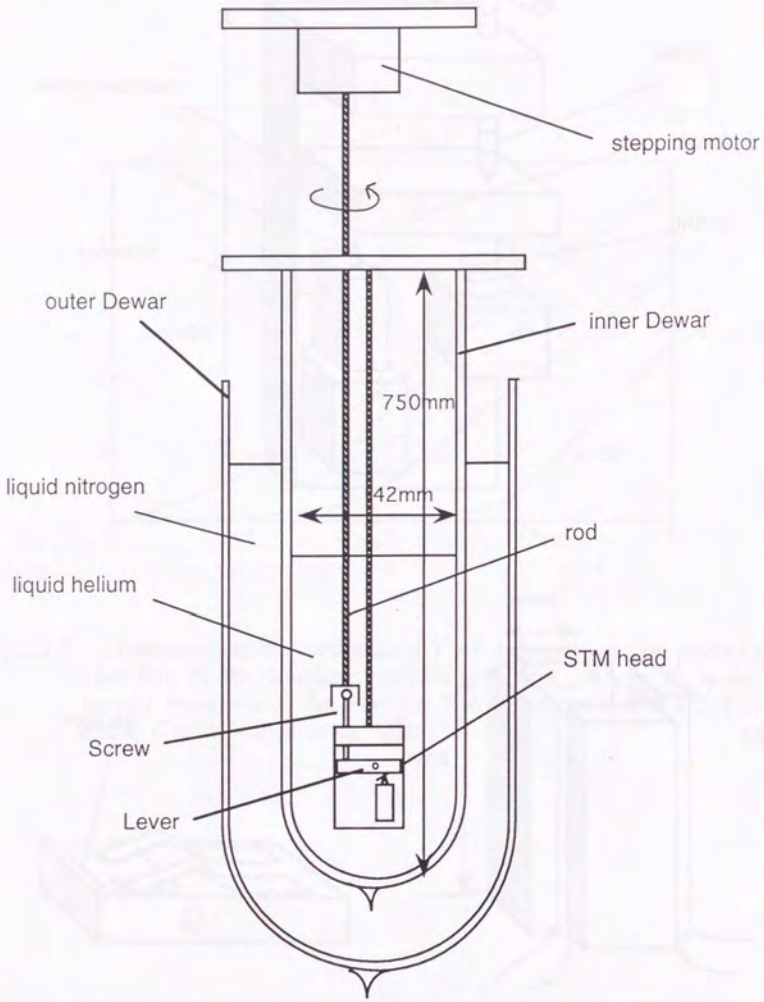


**Fig3.1.2** Schematic view of the approach mechanism and the cryostat

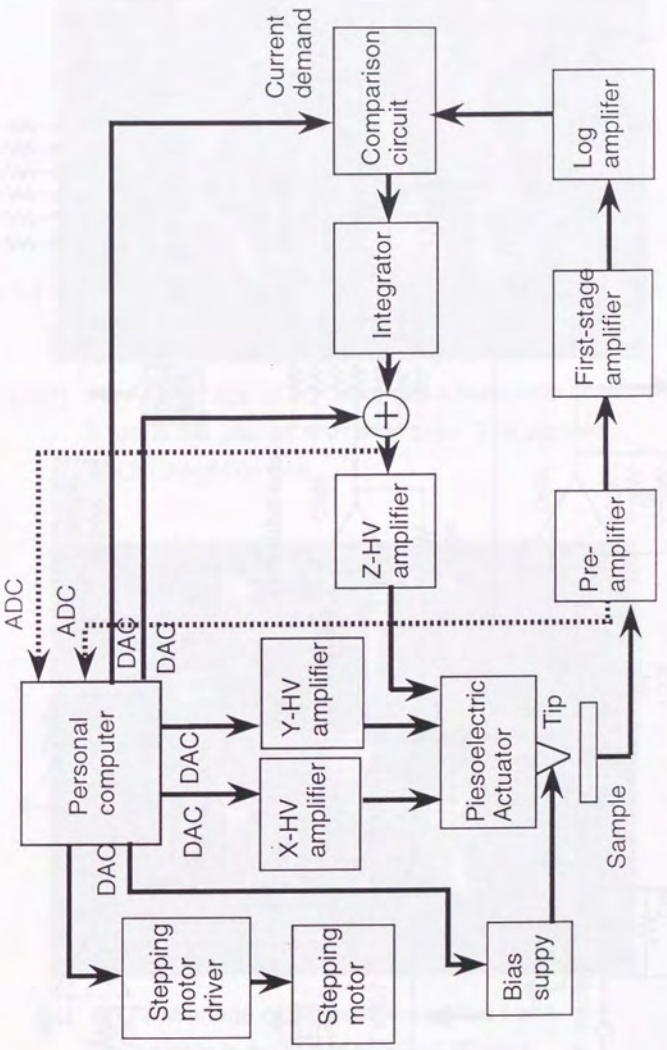


**Fig.3.2.1** Circuit diagram of STM

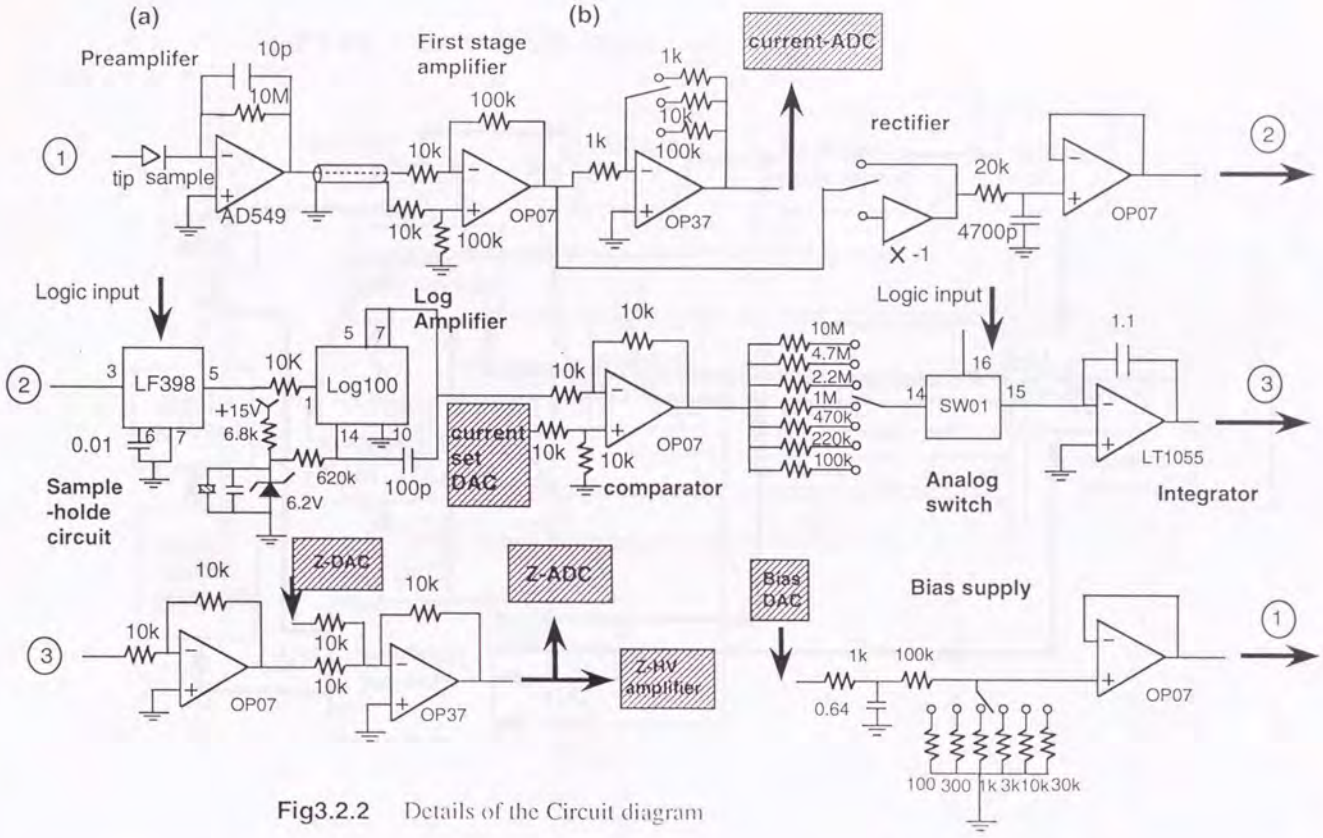


Fig3.2.2 Details of the Circuit diagram

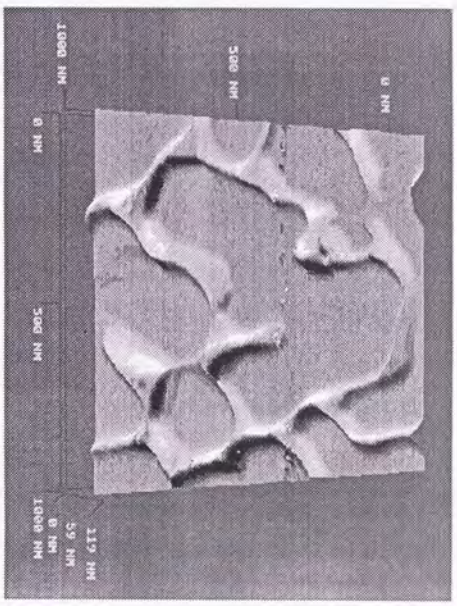

Fig. 4.1.1(a) An AFM image of Ag base with a thin oxide layer. It forms flat planes with wide area. The sample is $Al_2O_310/Ag500/mica$.

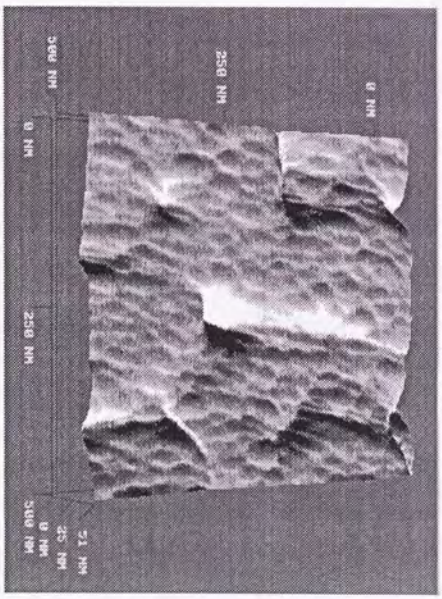

(b) An AFM image of Ag particles on the base. The sample is $Ag30/Al_2O_312/Ag570/mica$.

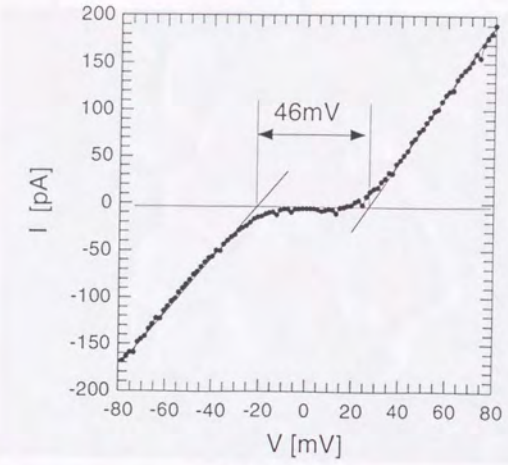


Fig.5.1.1 *I-V* characteristics measured by STS at 4.2K. It shows the Coulomb blockade feature. The sample is Au10 Å/$Al_2O_3$10 Å/Au500 Å.

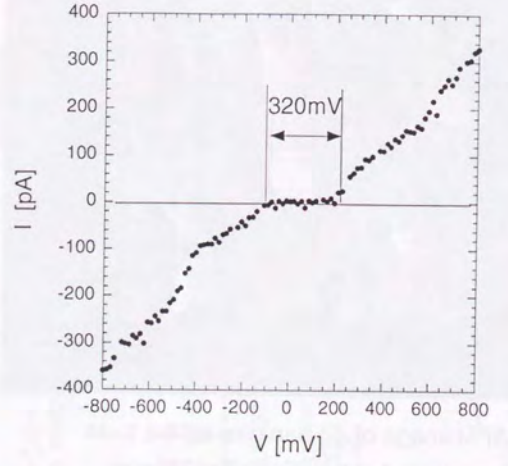


Fig.5.1.2 *I-V* characteristics measured by STS at 4.2K. It shows the Coulomb staircase. The sample is Au10 Å/$Al_2O_3$10 Å/Au500 Å.

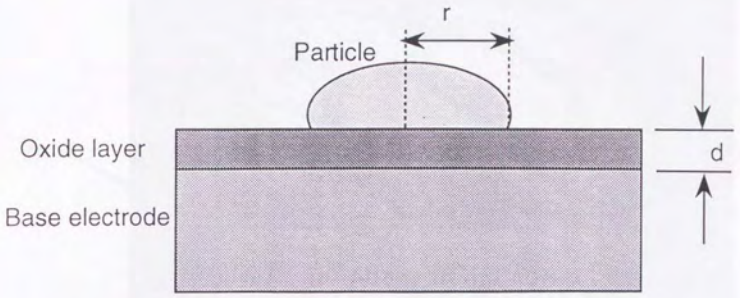


**Fig.5.1.3** A parallel capacitor model for estimating a particle radius *r* from a Coulomb blockade offset voltage *Voff*. The oxide layer is *d* in thickness.

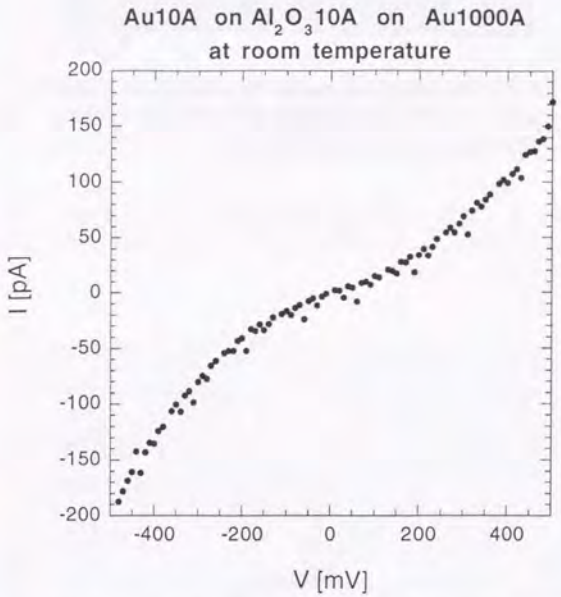


Fig.5.1.4 I-V characteristics measured by STS at room temperature. Current is suppressed around zero bias voltage owing to the Coulomb blockade.

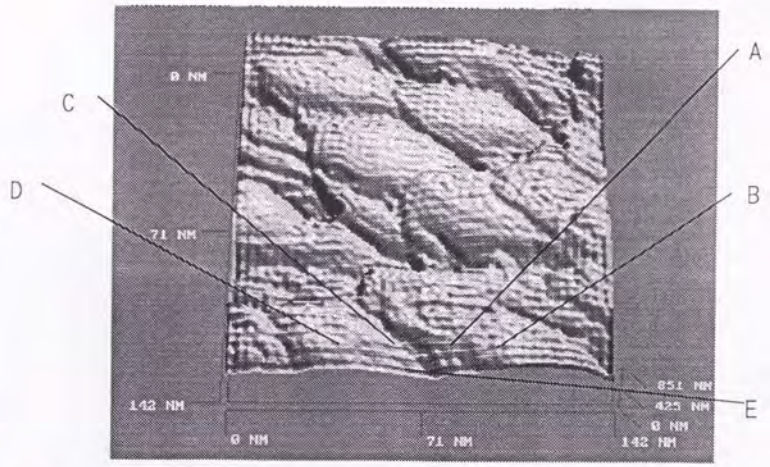


Fig.5.1.5(a) An STM image of Ag grains taken at 4.2K before STS. The sample is Ag30/$Al_2O_3$12/Ag550.

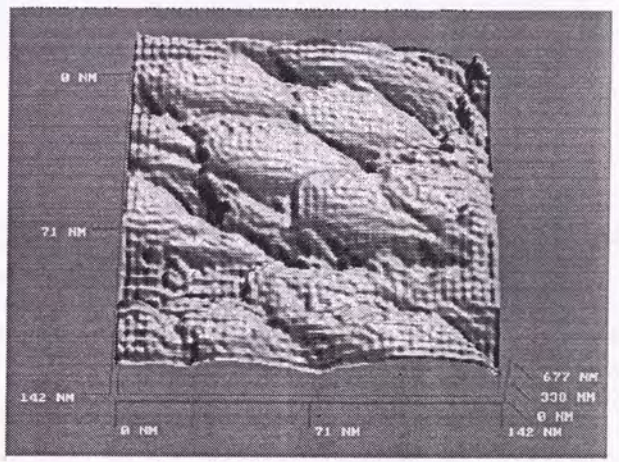


(b) An STM image of Ag grains taken at 4.2K after STS. The sample is the same as that of (a).

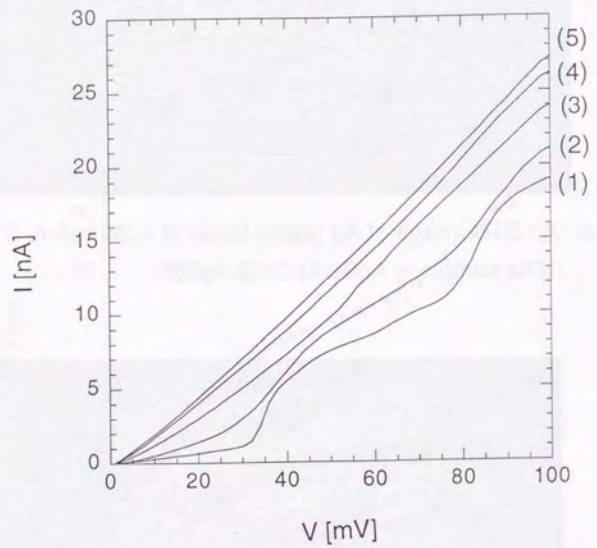


Fig.5.1.6 Changes of *I-V* characteristics caused by tip- sample approach. The STM tip was moved to the sample by 9 Å after one *I-V* characteristics is obtained, and this process was repeated five times. The number (1)-(5) denote the sequence of the measurements.

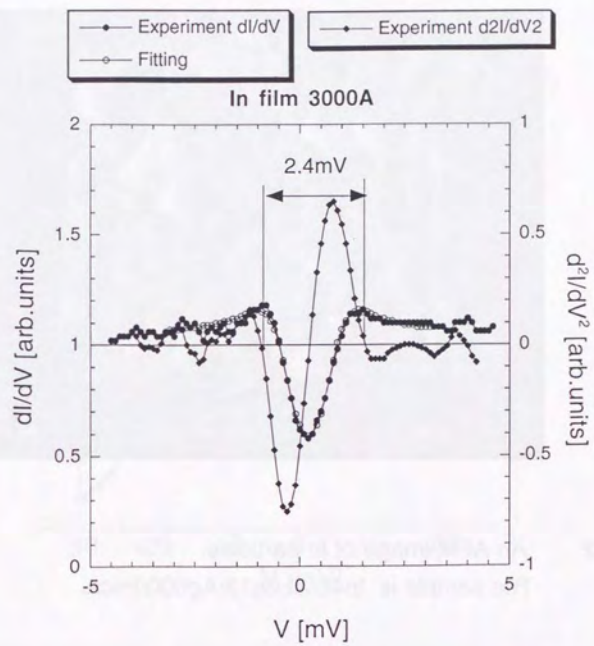


Fig.5.2.1 Superconducting energy gap of an In thin film with a thickness of 3000 Å measured by STS. A fitting to a calculation that takes into acount finite life time of quasi particles is also shown.

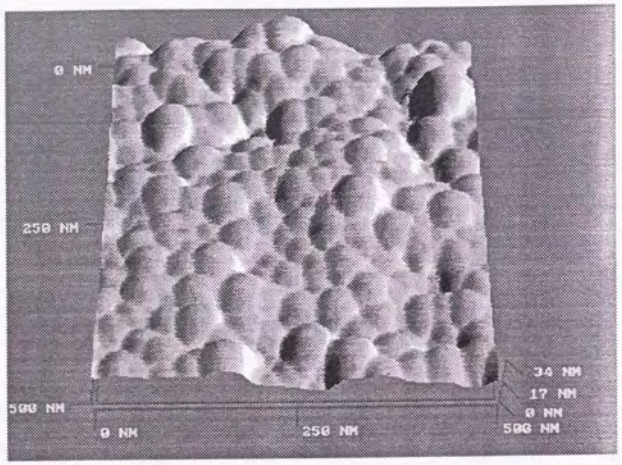


Fig.5.2.2 An AFM image of In particles.
The sample is In40/$Al_2O_3$13/Ag600/mica.

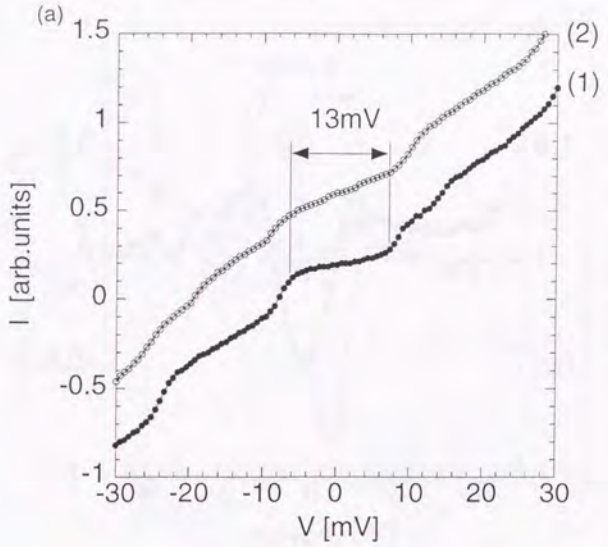


Fig.5.2.3 STS measurements of an In fine particle at 1.6 K.
(a) *I-V* characteristics for different distances between the tip and the particle. The distance was controlled by the set current when the feedback loop was closed. Each curve is normalized by the current at 30 meV and displaced vertically for clarity.
The set current is (1) 410 pA at 30 mV (2) 780 pA at 30 mV.

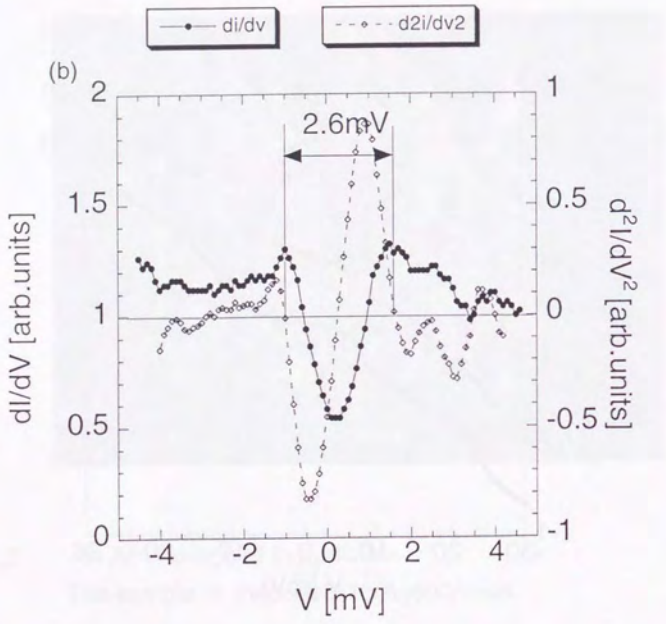


(b) $dI/dV$-$V$ characteristics and $d^2I/dV^2$-$V$ characteristics for (a)-(2).

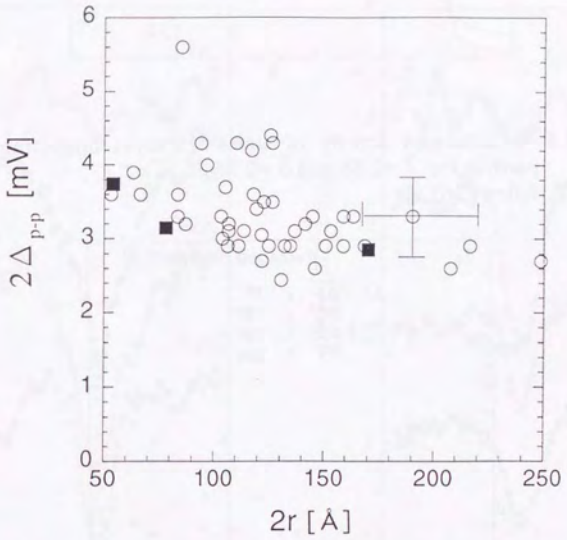


Fig.5.2.4 Dependence of the spacing between the peaks $2\Delta_{p\text{-}p}$ in a spectrum of an In particle on its diameter $2r$ (open circles). Those calculated from Sone's theory is also plotted (closed square).

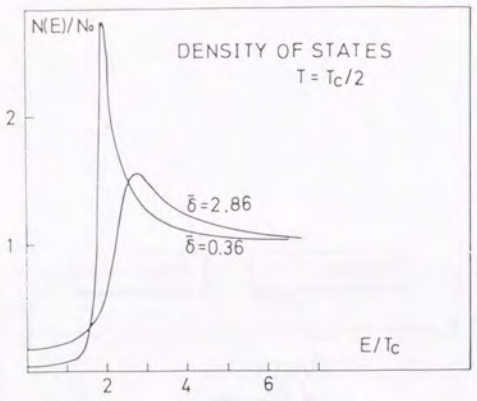


Fig.5.2.5 Calculated density of states of a superconducting fine particle for $\bar{\delta}$ =2.86 and $\bar{\delta}$ =0.36 at $T=T_c/2$. After [36].

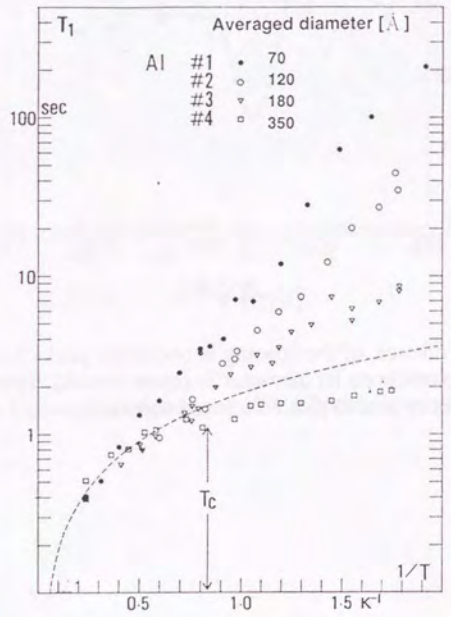


Fig.5.2.6 Temperature dependence of the nuclear spin-lattice relaxation time $T_1$ of Al particles. After [13].

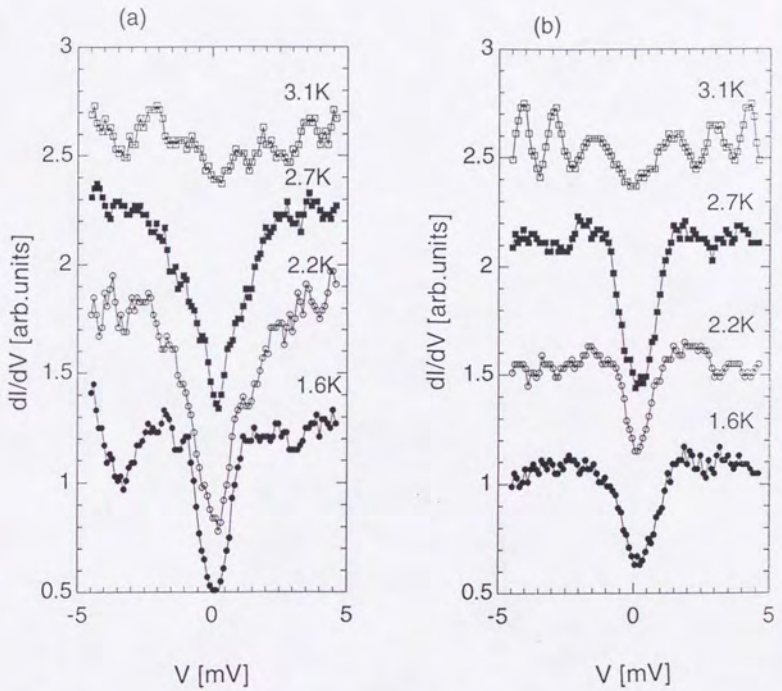


Fig.5.2.7 Temperature dependence of energy spectra measured by STS for (a) an In fine particle and (b) an In thin film. From bottom to top, temperature is varied as T=1.6K, 2.2K, 2.7K, and 3.1K. Each curve is normalized by the value at 5mV and displaced vertically for clarity.